Nonequilibrium atmospheric secondary organic aerosol formation and growth

Véronique Perraud[a], Emily A. Bruns[a], Michael J. Ezell[a], Stanley N. Johnson[a], Yong Yu[a,1], M. Lizabeth Alexander[b], Alla Zelenyuk[b], Dan Imre[c], Wayne L. Chang[d], Donald Dabdub[d], James F. Pankow[e], and Barbara J. Finlayson-Pitts[a,2]

[a]Department of Chemistry, University of California, Irvine, CA 92697-2025; [b]Pacific Northwest National Laboratory, P.O. Box 999, Richland, WA 99352; [c]Imre Consulting, 181 McIntosh Court, Richland, WA 99352; [d]Department of Mechanical and Aerospace Engineering, University of California, Irvine, CA 92697-3975; and [e]Department of Chemistry, Portland State University, Portland, OR, 97207

Contributed by Barbara J. Finlayson-Pitts, December 14, 2011 (sent for review September 28, 2011)

Airborne particles play critical roles in air quality, health effects, visibility, and climate. Secondary organic aerosols (SOA) formed from oxidation of organic gases such as α-pinene account for a significant portion of total airborne particle mass. Current atmospheric models typically incorporate the assumption that SOA mass is a liquid into which semivolatile organic compounds undergo instantaneous equilibrium partitioning to grow the particles into the size range important for light scattering and cloud condensation nuclei activity. We report studies of particles from the oxidation of α-pinene by ozone and NO_3 radicals at room temperature. SOA is primarily formed from low-volatility ozonolysis products, with a small contribution from higher volatility organic nitrates from the NO_3 reaction. Contrary to expectations, the particulate nitrate concentration is not consistent with equilibrium partitioning between the gas phase and a liquid particle. Rather the fraction of organic nitrates in the particles is only explained by irreversible, kinetically determined uptake of the nitrates on existing particles, with an uptake coefficient that is 1.6% of that for the ozonolysis products. If the nonequilibrium particle formation and growth observed in this atmospherically important system is a general phenomenon in the atmosphere, aerosol models may need to be reformulated. The reformulation of aerosol models could impact the predicted evolution of SOA in the atmosphere both outdoors and indoors, its role in heterogeneous chemistry, its projected impacts on air quality, visibility, and climate, and hence the development of reliable control strategies.

atmospheric aerosol | nitrate radical | kinetic growth mechanism | condensation mechanism

Airborne particles are well-known to negatively affect human health (1) and to contribute to "haze" associated with urban and regional pollution, leading to a reduction in visibility (2). On a global scale, airborne particles scatter solar radiation and can act as cloud condensation (CCN) and ice nuclei (IN), influencing the radiative balance of the atmosphere (3, 4). Currently these effects represent the largest uncertainty in calculations of climate change (5). A major component of atmospheric particles is secondary organic aerosol (SOA) formed via the oxidation of gaseous anthropogenic and biogenic precursor compounds. The SOA material is formed from low-volatility oxidation products (3, 4). However, the processes and species leading to SOA formation and growth are not fully understood, which precludes reliable quantitative predictions of their impacts on climate, visibility, and human health.

Regional and global chemical models have generally underpredicted SOA concentrations compared to those from field measurements (6–9). Inclusion of a number of additional factors such as new SOA precursors, condensed phase chemistry, updated gas-phase chemistry and SOA yields, new primary semivolatile and intermediate volatility species, and improved emissions inventories of both gases and primary organic aerosols have lessened the magnitude of the disagreement (10–18). However, there is still significant uncertainty in predicting ambient SOA levels, and model-measurement discrepancies of a factor of two or more remain common.

One possible source of this uncertainty is that current models typically assume instantaneous equilibrium partitioning of semivolatile organic compounds (SVOCs) between existing liquid airborne particles and the gas phase using the theory of absorptive, activity coefficient-corrected, gas/liquid partitioning described in detail by Pankow (19, 20). Equilibrium partitioning is justified for particles with viscosities in the range of 0.01–100 Pa · s and diffusion coefficients ranging from 10^{-5} to 10^{-9} $cm^2\,s^{-1}$ (21). A volatility basis set approach has recently been developed for representing the partitioning of SVOCs, which also depends on saturation mass concentration of liquid particles (22).

In this paper, we present laboratory studies of particles formed in the simultaneous oxidation of α-pinene by ozone and NO_3 radicals using an aerosol flow system (23). Quantification of the organic nitrate contributions to the SOA provides unique insight into the mechanisms by which particles form and grow, which has important implications for model formulations of SOA, both outdoors and indoors, and the associated impacts predicted based on the model outputs.

Results and Discussion

Oxidants (O_3 and NO_2) are well mixed in the upstream end of an aerosol flow tube (8.5 m in length, 0.5 m in diameter) described in detail elsewhere (23). The reaction of NO_2 with O_3 forms NO_3 radicals which are mainly "stored" as N_2O_5 (see *SI Text*): $NO_2 + NO_3 \rightleftharpoons N_2O_5$. After approximately 4 min reaction time, α-pinene is injected. Experiments are performed at relative humidity (RH) < 3% without preexisting seed particles. Reactants, gas-phase products, and SOA then flow into the sampling section of the flow tube, which is equipped with five equally spaced ports (port 1 to port 5). Port 1 corresponds to a reaction time between α-pinene and the $NO_2/O_3/N_2O_5$ mixture of approximately 13 min, whereas port 5 corresponds to a reaction time of approximately 52 min. Most of the experimental data presented hereafter are taken at port 5; no major differences are observed in the SOA measurements between port 1 and port 5, establishing that the chemistry is essentially complete by port 1 and the particles travel along the length of the flow tube to port 5 without further significant modification or "aging." Integration of the rate equations for a simplified mechanism for this system (see *SI Text*) shows that the NO_3 chemistry is the dominant oxidation process for α-pinene under all experimental conditions, and is sufficiently rapid

Author contributions: V.P., M.J.E., S.N.J., D.D., and B.J.F.-P. designed research; V.P., E.A.B., M.J.E., S.N.J., Y.Y., M.L.A., A.Z., W.L.C., D.D., and B.J.F.-P. performed research; V.P., E.A.B., M.J.E., S.N.J., A.Z., D.I., W.L.C., D.D., J.F.P., and B.J.F.-P. analyzed data; and V.P., A.Z., D.D., J.F.P., and B.J.F.-P. wrote the paper.

The authors declare no conflict of interest.

[1]Present address: California Air Resources Board, 9528 Telstar Avenue, El Monte, CA 91731.

[2]To whom correspondence should be addressed. E-mail: bjfinlay@uci.edu.

This article contains supporting information online at www.pnas.org/lookup/suppl/doi:10.1073/pnas.1119909109/-/DCSupplemental.

($k^{NO_3} = 6.2 \times 10^{-12}$ cm^3 molecule^{-1} s^{-1}; ref. 24) so that the reaction is >90% complete in terms of α-pinene loss by port 1 (Table S1). This loss is confirmed by experimental measurements of α-pinene by GC-MS. The validity of the kinetics model is also verified by using the model-predicted concentrations of NO_3 and N_2O_5 (Fig. S1) to predict how much organic nitrate should be formed and by comparing these concentrations to those measured using FTIR (Fig. S2).

The size distributions of SOA formed by the oxidation of α-pinene are shown in Fig. 1 (and Fig. S3) when NO_2 is varied from 6.3 to 0 ppm at constant O_3. At the highest NO_2 concentration, few particles are formed, which is expected because multifunctional organic nitrates, formed in the NO_3 reaction with α-pinene, have sufficiently high vapor pressures that they do not readily nucleate to form new particles (25–27). For example, the products 3-oxopinane-2-nitrate, 2-hydroxypinane-3-nitrate, and pinonaldehyde peroxyacetyl nitrate, which have been measured in the gas phase (27–30) with an average total yield of 16.5%, have vapor pressures between 4×10^{-6} and 1×10^{-7} atm at 295 K (26, 31). However, ozonolysis products typically have lower vapor pressures (e.g., *ca.* 1×10^{-7} and 6×10^{-10} atm for pinonic and pinic acids, respectively; ref. 31) and more readily undergo homogeneous nucleation to form new particles. As the NO_2 concentration decreases and the contribution of O_3 to the α-pinene loss increases, the particle number and mass concentration due to ozonolysis increase (Fig. 1 and Fig. S4) as expected.

Organic nitrate products from the NO_3 chemistry comprise a fraction of the SOA. For example, Fig. 2 shows FTIR spectra from particles collected at the end of the flow tube as a function of initial NO_2 concentration. In addition to the aliphatic −C–H stretches in the 2,800–3,000 cm^{-1} region, three infrared bands corresponding to the $-ONO_2$ asymmetric stretch (1,630 cm^{-1}), the $-ONO_2$ symmetric stretch (1,280 cm^{-1}), and RO–NO_2 stretch (860 cm^{-1}) characteristic of organic nitrates are seen (27, 29, 32–34). As described in the *SI Text*, these spectra show that the relative number of $-ONO_2$ groups to −C–H groups, $n_{(-ONO_2)}/n_{(-CH)}$, increases with the NO_2 concentration (Table S2).

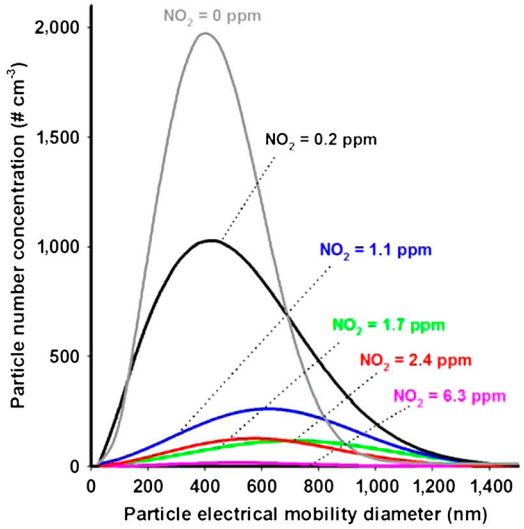

Fig. 1. Combined scanning mobility particle sizer (SMPS)–aerodynamic particle sizer size distributions of particles as a function of NO_2 concentration from 6.3 to 0.2 ppm, with a constant 1.4 ppm concentration of O_3. The gray trace is that for reaction with 1.6 ppm O_3 alone. All traces correspond to the Weibull fit; Fig. S3 presents the experimental data and this fit. Measurements were made at port 5 of the flow tube (*ca.* 52 min reaction time between α-pinene and the $NO_2/O_3/N_2O_5$ mixture) except for the blue trace (NO_2 = 1.1 ppm) where only SMPS data from port 1 were available (*ca.* 13 min reaction time between α-pinene and the $NO_2/O_3/N_2O_5$ mixture). However, when simultaneous measurements were made at port 1 and port 5 for the $NO_2 + O_3$ system, the measured distributions were similar.

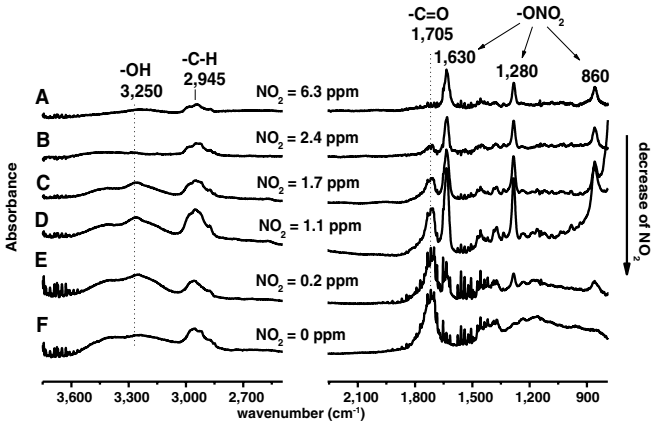

Fig. 2. FTIR spectra from particles collected on ZnSe discs (50% cut point at 0.5 μm for 9 L min^{-1} flow rate through the impactor; spectra for a 1.0-μm cutoff disc are similar) as a function of the NO_2 concentration from 6.3 to 0.2 ppm (*A–E*) with an initial O_3 concentration of 1.4 ppm. *F* is from the ozonolysis experiment using 1.6 ppm O_3. Because no attempt was made to collect the same mass of SOA for each sample, it is the relative peak heights for the $-ONO_2$ groups compared to the −C–H bands that indicate the trends in organic nitrate products with the initial NO_2 concentration, rather than the absolute peak heights.

Similarly, mass spectra acquired using real-time high-resolution time-of-flight mass spectrometry (HR-TOF-AMS) and single particle mass spectrometry (SPLAT-II) show that the SOA contains organic nitrates (Fig. S5). The spectra when NO_2 is present (Fig. S5 *A–C* and *E–G*) are very similar to those for the ozonolysis reaction (Fig. S5 *D* and *H*), except that peaks at m/z 30 and 46 also appear, primarily from NO^+ and NO_2^+ (SPLAT-II spectra show primarily m/z 30). The NO^+/NO_2^+ ratio from the high-resolution AMS mass spectra ranges from 4.9 to 7.6, consistent with a contribution from organic nitrate products (35–38) from the NO_3 reaction with α-pinene (26, 27, 35).

The similarity of the spectra in the presence and absence of NO_2 suggests that the overall bulk composition of the aerosol (excluding the organic nitrate component) remains relatively constant. For example, the O:C ratios calculated from the AMS data (Fig. S6) average 0.34 ± 0.10 over the range of experimental conditions. This average value is similar to previous measurements of SOA from α-pinene ozonolysis (39–41) and with pinonic and pinic acid (with O:C ratios of 0.3 and 0.4, respectively), which are known to be major products of the ozone reaction (42, 43). Although there may be a slight trend in the O:C ratio with the NO_2 concentration, it is not significant within uncertainty of the measurements.

Extracts of particles collected on quartz-fiber filters are analyzed by liquid chromatography with UV detection (LC-UV). Chromatograms (Fig. S7) show a group of overlapping peaks with UV spectra attributable to organic nitrates (44) in all NO_2 experiments. The mass concentrations of total organic nitrates in the particles derived from the LC-UV data (F_i, μg per m^3 of air) (see Eq. **S5**) are shown in Table 1 as a function of the initial NO_2 concentration. Using the size distributions and the densities measured by SPLAT-II, the total mass concentration of particles and the mass fraction of organic nitrates (f_{APONO2}) are also calculated. Organic nitrates comprise between 0.1–8.2% of the total SOA mass and follow the trend in NO_2. This trend is also shown in the HR-TOF-AMS and FTIR analysis (Table S2).

In short, measurement of the SOA composition by three different techniques shows that the organic nitrate contribution to the SOA decreases as the NO_2 concentration (and thus the available NO_3 radicals to react with α-pinene) decreases. Simultaneously, the amount of SOA formed increases due to the increasing contribution of the O_3 reaction. Fig. 3 summarizes qualitatively the chemistry occurring in this system: Although ozonolysis is primarily

Table 1. Total and particulate organic nitrate concentrations and total mass concentrations of SOA

Initial $[NO_2]_0$, 10^{14} molecules cm^{-3} or [ppm]	Mass concentration of total organic nitrates [APONO2],* μg per m^3 of air	Mass concentration of aerosol organic nitrates F_i,† μg per m^3 of air	Total mass concentration of SOA M,‡ μg per m^3 of air	f_{APONO2}, %
		NO_3 experiments, with $[O_3]_o = 1.4$ ppm		
1.6 [6.3]	394	2.3	28	8.2
0.59 [2.4]	319	7.6	392	1.9
0.42 [1.7]	270	8.0	436	1.8
0.27 [1.1]	195	5.0	907	0.6
0.05 [0.2]	42	1.1	1,791	0.06
		O_3 experiments, with $[O_3]_o = 1.6$ ppm		
0.00		0	1,948	0

Measured at a reaction time of 52 min corresponding to the fifth and last port of the flow tube (see *SI Text*).

*From the box model. The output of the model corrected for N_2O_5 wall loss, [APONO2], in molecules cm^{-3}, is converted into a mass concentration using $MW_{APONO2} = 220$ g mol^{-1} (26).

†From LC-UV data (see *SI Text*).

‡From scanning mobility particle sizer–aerodynamic particle sizer composite size distributions and densities measured by SPLAT-II (see *SI Text*).

responsible for SOA formation, ozonolysis products (hereafter defined as "Prod1") and organic nitrates (hereafter defined as "APONO2") are both incorporated into the SOA, contributing to its growth.

To probe the chemistry quantitatively, a simplified 96-step mechanism for the $NO_2 + O_3 + \alpha$-pinene system is developed, and the rate equations are integrated using Acuchem (45). Two reaction channels are assumed for the NO_3 reaction and two for the O_3 reaction:

$$\alpha\text{-pinene} + NO_3 \rightarrow \text{APONO2}$$
$$k_1 = 1.0 \times 10^{-12}\ \text{cm}^3\ \text{molecule}^{-1}\ \text{s}^{-1} \quad [1]$$

$$\rightarrow \text{other products}$$
$$k_2 = 5.2 \times 10^{-12}\ \text{cm}^3\ \text{molecule}^{-1}\ \text{s}^{-1} \quad [2]$$

$$\alpha\text{-pinene} + O_3 \rightarrow OH + RO_2$$
$$k_3 = 7.4 \times 10^{-17}\ \text{cm}^3\ \text{molecule}^{-1}\ \text{s}^{-1} \quad [3]$$

$$\rightarrow \text{Prod1}$$
$$k_4 = 1.6 \times 10^{-17}\ \text{cm}^3\ \text{molecule}^{-1}\ \text{s}^{-1}. \quad [4]$$

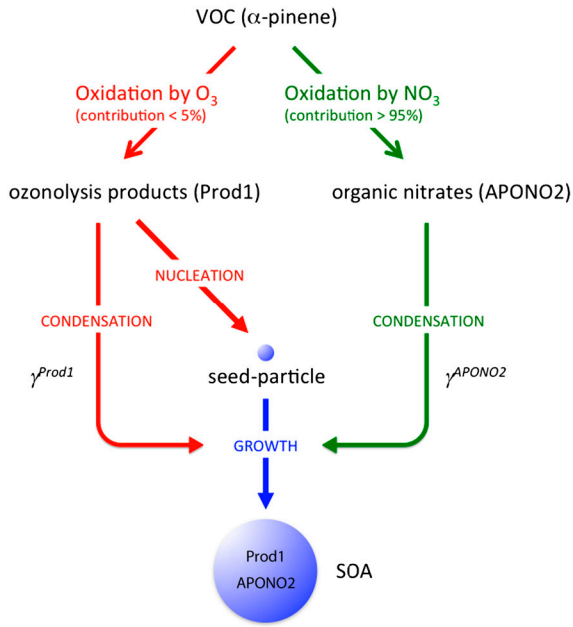

Fig. 3. Representation of SOA formation and growth based on the experimental observations. See text for details.

The rate constants for these reactions are based on known rate constants for the overall reactions (24) and branching ratios for the formation of organic nitrates (APONO2) and OH radicals. Thus, the yield of organic nitrates in the NO_3 reaction is taken to be 16.5% (46) and the OH yield in the ozone reaction is taken to be 82% (46). Prod1 is a marker for the O_3 chemistry that represents, in part, low-volatility products that lead to particle formation and growth. The use of a first-generation product (Prod1) as a proxy for SOA is supported by the work of Ng et al. (47) who showed that the particles from α-pinene ozonolysis are due to first-generation low-volatility products. Fig. S2 compares the box model-predicted total (gas plus particle phase) concentrations of APONO2 as a function of the initial NO_2 (gray dashed line) to the gas-phase organic nitrate concentrations measured using long-path FTIR (black circles). This comparison should be reasonable because most of the organic nitrates are in the gas phase (Table 1). As described in the *SI Text*, the model well represents the time evolution of the total concentration of organic nitrates as a function of the initial NO_2 concentration.

Growth of SOA has often been described via *ad*sorption of SVOCs, such as organic nitrates, onto the particle surface or *ab*sorption into the bulk. In most atmospheric models of SOA, the latter process (19, 20) is taken to be responsible for uptake of SVOCs into existing liquid particles. It is assumed that once a seed particle is formed (e.g., by homogeneous nucleation), SVOCs will partition into the bulk liquid phase of the particles, causing it to grow.

An equilibrium partitioning coefficient ($K_{p,i}$) for compound i is defined as the ratio of the concentrations of compound i in the gas and particle phases, assuming a reversible gas-particle partitioning based on Raoult's law with activity corrections (19, 20):

$$K_{p,i} = \frac{F_i/M}{A_i} = \frac{f_{om}RT}{MW_{om}10^6\xi_i p^0_{L,i}}. \quad [5]$$

In Eq. **5**, F_i and A_i are the mass concentrations (μg per m^3 of air) of compound i in the aerosol and gas phase, respectively, and M (μg per m^3 of air) is the mass concentration of particulate material, so $K_{p,i}$ has units of m^3 per μg. On the right-hand side of Eq. **5**, f_{om} is the mass fraction of the presumably largely organic material portion of the particulate matter into which the partitioning is occurring (because of the absence of preexisting seed particles, f_{om} is unity for our experiments), R is the ideal gas constant (m^3 atm K^{-1} mol^{-1}), T is the temperature (K), MW_{om} (g mol^{-1}) is the average molecular weight of the particulate matter phase into which the partitioning is occurring, ζ_i is the activity coefficient of compound i, and $p^0_{L,i}$ is the vapor pressure of compound i (atm).

Values of F_i/M and A_i for the sum of all organic nitrates are calculated using F_i and M from Table 1, and the corrected gas-

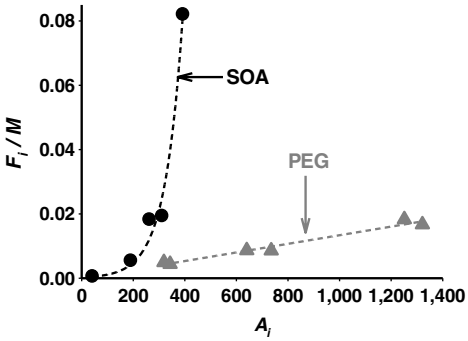

Fig. 4. Dependence of F_i/M on A_i (see text for definitions) for organic nitrates in SOA from the oxidation of α-pinene by O_3/NO_2 for the flow tube experiments (black circles), and in the PEG seed particle experiments (gray triangles). (The total mass concentration of PEG particles is approximately 5,000 $\mu g\, m^{-3}$).

phase concentrations (A_i; see *SI Text*) from the box model with $A_i = [\text{APONO2}] - F_i$. Eq. **5** predicts that a plot of F_i/M versus A_i will be a straight line with slope K_p, which is seen in Fig. 4 (black circles) not to be the case for the $NO_2/O_3/\alpha$-pinene system.

There are four possible sources of this unexpected variation that are associated with the physical description of K_p (right-hand side of Eq. **5**): (*i*) The activity coefficients (ζ_i) vary systematically as the NO_2 concentration changes; (*ii*) the gas-phase box model does not predict accurately A_i as a function of NO_2 concentration; (*iii*) the composition of the SOA into which the organic nitrates partition changes dramatically with NO_2 concentration; or (*iv*) the conditions for which Eq. **5** is developed do not apply in this system. As shown in Fig. S5 and discussed in the *SI Text*, a systematic variation in the bulk SOA composition (excluding the organic nitrates) and hence in ζ_i is unlikely. With respect to (*ii*), experimental measurements of gas-phase organic nitrates show that the box model does predict accurately their trend with NO_2 (Fig. S2). The third possibility is ruled out by the data presented in Figs. S5 and S6, which show that the SOA composition does not change significantly, except for the contribution of organic nitrates (see discussion above). This process of elimination leaves the fourth possibility—i.e., that the equilibrium described by Eq. **5** does not apply in this system.

To test that organic nitrates do partition into particles that are known to be liquid and where equilibrium should be rapidly achieved, uptake into liquid poly(ethylene glycol) (PEG) particles (see *SI Text*) is studied. Organic nitrates are generated in a separate set of experiments by reacting α-pinene with NO_3, generated from the thermal decomposition of varying concentrations of N_2O_5. The mixture of products and remaining reactants are then exposed to PEG particles. After approximately 10 min, particles are collected and analyzed using the same technique as for the $NO_2/O_3/\alpha$-pinene experiments. Fig. 4 (gray triangles) shows that F_i/M depends linearly on A_i, consistent with equilibrium partitioning into liquid particles as described by Eq. **5**. This outcome is not surprising; for a liquid of the viscosity of the PEG (*ca.* 0.1 Pa · s), the diffusion coefficient is approximately $5 \times 10^{-6}\ cm^2\, s^{-1}$ and the time to diffuse from the surface to the center of a 260-nm diameter particle (average geometric mean diameter of the PEG particle distributions) is only about 35 μs (21).

In short, although the organic nitrates partition in equilibrium fashion as expected into liquid PEG particles, the same is not the case for the incorporation of organic nitrates into the SOA formed in the ozonolysis of α-pinene, at least on the timescale (*ca.* 10–60 min) of the experiments.

An alternative hypothesis to equilibrium partitioning is that the particles grow and incorporate organic nitrates via a nonequilibrium, kinetically limited mechanism, similar to what has been described historically as a "condensation" mechanism (3, 4). Gas molecules impinge on the surface of an existing particle, with some probability that they will be taken up. This probability, and the time they remain adsorbed on the surface, are determined by the nature of the attractive forces operating between the gas and the surface of the particle. In addition, reactions at the surface that convert the adsorbate to lower volatility compounds (for example, oligomer formation) may contribute (48–51). If the residence time on the surface is sufficiently long, the adsorbed species can become "buried" and hence incorporated into the bulk by semivolatile gaseous compounds that subsequently condense. Based on gas kinetic theory, the time between collisions of a gas molecule with a molecular weight of 220 $g\, mol^{-1}$ with an adsorbed surface molecule is about 100 ms, assuming a 10 ppb gas-phase SVOC concentration and surface area per molecule of 1 nm^2. If a molecule at the surface has a longer residence time than 100 ms, the probability of it becoming buried by an incoming product molecule becomes significant. An estimate of reasonable residence times on the surface can be obtained from the rate constant for desorption (52), $k_{des} = Ae^{-E_a/RT}$ where $E_A \sim \Delta H_{sub}$ (or ΔH_{vap}, depending on the process). Heats of sublimation for acids and diacids are typically about 150 $kJ\, mol^{-1}$ (53, 54) and heats of vaporization and sublimation for simple alcohols are typically in the range of 80–120 $kJ\, mol^{-1}$ (55). Using $A \sim 10^{13}\ s^{-1}$, lifetimes on the surface will range from 10 to 10^{13} s, more than sufficient to be buried by incoming SVOCs.

To assess if this growth mechanism is consistent with the experimental data, the uptake of APONO2 and Prod1 are treated as irreversible and occurring with uptake probabilities of γ^{APONO2} and γ^{Prod1}. A value of the relative uptake coefficients, $\gamma^{\text{APONO2}}/\gamma^{\text{Prod1}} = 0.016$, is found to provide an excellent fit to the experimentally measured mass fraction of organic nitrates in the SOA (f_{APONO2}, Table 1) for all NO_2 concentrations (Fig. S8). These results show that a nonequilibrium kinetically determined mechanism determines the formation and growth of SOA in this atmospherically important system.

A kinetics mechanism implies that reevaporation of the organic nitrates back to the gas phase is negligible, at least on the timescale of these experiments. Given the earlier discussion of diffusion times under typical liquid viscosities (21), the lack of reevaporation shows that the SOA material must be very viscous; once the organic nitrate is buried, it does not readily diffuse back to the particle surface and into the gas phase. The characteristic times for diffusion in a 400-nm diameter particle for a liquid are 10 μs to 10 ms for diffusion coefficients in the range of 10^{-5} to $10^{-9}\ cm^2\, s^{-1}$ (21). For the approximately 1 h residence time in our flow system, equilibrium should be reached if the diffusion coefficient was $\geq 10^{-14}\ cm^2\, s^{-1}$. The fact that our data show equilibrium is not reached is compatible with the SOA being solid or semisolid, where $D < 10^{-14}\ cm^2\, s^{-1}$ (21). Clearly, the phase of a particle is important as it impacts the interaction of gas-phase products with the seed particles, and thus their growth rate, optical properties, and CCN activity (56).

Many studies have examined the timescales for the various steps associated with the formation and growth of SOA (21, 57–60); the conclusion is that the time for gas-phase SVOCs to come to equilibrium with *liquid* particles under typical atmospheric conditions is sufficiently short that the assumption of instantaneous equilibrium partitioning in atmospheric models is justified. However, a variety of recent results from other laboratories indicate that SOA in both ambient air and laboratory systems from reactions such as O_3 with α-pinene does not always behave like a liquid. Vaden et al. (61) show that SOA mixed with a hydrophobic liquid organic forms layered particles with SOA at the core coated with the hydrophobic organic, or a hydrophobic core coated with SOA, both of which were stable for many hours. Vaden et al. (62) also demonstrate that evaporation of ambient SOA particles from Sacramento, California as well as laboratory-generated SOA, is quite slow, and the size dependence of the eva-

poration is not consistent with that expected for liquid particles. Earlier studies of the desorption of organics from particles collected in a highway tunnel showed that the diffusion coefficients were orders of magnitude smaller than expected for liquids (63). Virtanen et al. (64, 65) report that particles collected in Hyytiälä, Finland and those generated in the laboratory by ozonolysis of α-pinene, bounce off impactor plates as if they are solids. Pierce et al. (66) show that freshly nucleated particles from Hyytiälä, Finland and Egbert, ON, Canada have very low volatility. Cappa and Wilson (67) demonstrate that the composition of SOA from the ozonolysis of α-pinene does not change with heating as expected if the evaporation is determined by equilibrium partitioning between a liquid particle and the gas phase. Thermodenuder measurements from field studies (11, 68) and laboratory-generated SOA from ozonolysis of monoterpenes (69, 70) show that thermal evaporation of the SOA (specifically at low RH) is much smaller than predicted by models of liquid particles, indicating that a significant fraction of the SOA is essentially nonvolatile.

Laboratory studies of the interaction of water vapor with some species relevant to atmospheric particles have also suggested that atmospheric particles may form highly viscous amorphous material under the appropriate conditions (71–73). More recently, Koop et al. (74) have shown that pinic acid and pinonic acid, which are major products of the α-pinene ozonolysis (42, 43), have glass transition temperatures between 265 and 268 K and thus can form a "glass" at lower temperatures found under some conditions in the troposphere; even above the glass transition temperature, the viscosity may be quite high.

In short, the results from our studies suggest that the assumption of instantaneous equilibrium commonly applied to SOA formation and evolution in most atmospheric models may need to be revisited. A kinetically limited/condensation growth mechanism actually can provide a better fit to field data. For example, measurements of the evolution of the number concentrations and size distributions of aerosols in the Mexico City area are shown to be consistent with a condensation mechanism for particle growth (75). Similarly, the growth of ultrafine aerosols from Egbert, ON, Canada and Hyytiälä, Finland are best modeled if >50% of the ultrafine particle growth was because of condensation (76). Very recent modeling efforts (77–79) also suggest the importance of this growth mechanism. As discussed in detail in the *SI Text*, the SOA measured in Riverside, California is consistent with a kinetically limited growth mechanism with no reevaporation if the overall average uptake coefficient for the SVOCs that lead to particle growth is of the order of 0.5–0.6.

The issue of thermodynamic equilibrium has also been discussed in detail with respect to modeling inorganic atmospheric aerosols. The first generation of aerosol models assumed thermodynamic equilibrium for the volatile compounds between the gas and aerosol phase (80–83). However, measurements by Tanner (84), Allen et al. (85), and Wexler and Seinfeld (86) showed that equilibrium is not always achieved, especially within the time step used by models. Consequently, gas-to-particle conversion for inorganic species is now generally represented in aerosol modules by a dynamic mass transfer between the gas and aerosol phases (e.g., Meng et al., ref. 87).

In short, the combination of experiments reported here suggests that uptake of SVOCs into ambient SOA is consistent with a kinetically limited/condensation growth mechanism. Adsorbed SVOCs become incorporated into the bulk by being buried by incoming gas molecules and do not reevaporate, at least on the timescale of the experiments. If this process proves to be a general phenomenon, then the current formation and growth of SOA is not appropriately represented in most atmospheric models that rely on instantaneous thermodynamic equilibrium of SVOCs into liquid particles. Thus, current treatments of SOA formation and growth in models for both indoor and outdoor environments and the predicted impacts based on these models may need to be revisited.

Materials and Methods

A brief description of the experimental procedure is provided below and details can be found in the *SI Text*. α-Pinene was reacted with mixtures of O_3 and NO_2 in an aerosol flow tube (23). The size distributions, densities, and composition of the particles formed were measured using a scanning mobility particle sizer, an aerodynamic particle sizer, two particle mass spectrometers (SPLAT-II-MS and HR-TOF-AMS), LC-UV, and FTIR. Gas-phase concentrations were measured using a chemiluminescence NO_x analyzer, a photometric O_3 analyzer, GC-MS, and long-path FTIR. For comparison, experiments were performed in Teflon reaction chambers using liquid PEG seed particles and the use of N_2O_5 as the source of NO_3 radicals.

ACKNOWLEDGMENTS. E.A.B. thanks the National Science Foundation for a Graduate Research Fellowship. We are also grateful to Paul Ziemann for discussions regarding organic nitrate analysis, and Sergey Nizkorodov, James N. Pitts, Jr., Margaret Tolbert, and Paul Shepson for comments on the manuscript. This work was funded by the US Department of Energy (DOE) (Grant DE-FG02-05ER64000) and the National Science Foundation (Grant CHE-0909227). This research was in part in collaboration with the Environmental Molecular Sciences Laboratory, a national scientific user facility sponsored by the US DOE's Office of Biological and Environmental Research at Pacific Northwest National Laboratory (PNNL) and supported by the US DOE's Office of Basic Energy Sciences, Chemical Sciences Division. PNNL is operated by Battelle Memorial Institute under Contract DE-AC06-76RL0 1830.

1. Pope CA, et al. (2002) Lung cancer, cardiopulmonary mortality, and long-term exposure to fine particulate air pollution. *J Am Med Assoc* 287:1132–1141.
2. Hinds WC (1999) *Aerosols Technology: Properties, Behavior and Measurement of Airborne Particles* (Wiley Interscience, New York), pp 364–370.
3. Finlayson-Pitts BJ, Pitts JN, Jr (2000) *Chemistry of the Upper and Lower Atmosphere—Theory, Experiments, and Applications* (Academic, San Diego), pp 349–435 pp 788–814.
4. Seinfeld JH, Pandis SN (1998) *Atmospheric Chemistry and Physics: From Air Pollution to Climate Change* (Wiley Interscience, New York), pp 700–751 pp 1113–1184.
5. Intergovernmental Panel on Climate Chang (2007) *IPCC, Climate Change 2007—The Physical Science Basis: Contribution of Working Group I to the Fourth Assessment Report of the IPPC* (Cambridge Univ Press, Cambridge, UK).
6. Volkamer R, et al. (2006) Secondary organic aerosol formation from anthropogenic air pollution: Rapid and higher than expected. *Geophys Res Lett* 33:L17811.
7. Hodzic A, et al. (2009) Modeling organic aerosols during MILAGRO: Importance of biogenic secondary organic aerosols. *Atmos Chem Phys* 9:6949–6982.
8. O'Donnell D, Tsigaridis K, Feichter J (2011) Estimating the direct and indirect effects of secondary organic aerosols using ECHAM5-HAM. *Atmos Chem Phys* 11:8635–8659.
9. Heald CL, et al. (2005) A large organic aerosol source in the free troposphere missing from current models. *Geophys Res Lett* 32:L18809.
10. Carlton AG, et al. (2010) Model representation of secondary organic aerosol in CMAQv4. *Environ Sci Technol* 44:8553–8560.
11. Dzepina K, et al. (2009) Evaluation of recently-proposed secondary organic aerosol models for a case study in Mexico City. *Atmos Chem Phys* 9:5681–5709.
12. Foley KM, et al. (2010) Incremental testing of the Community Multiscale Air Quality (CMAQ) modeling system version 4. *Geosci Model Dev* 3:205–226.
13. Hodzic A, et al. (2010) Modeling organic aerosols in a megacity: Potential contribution of semi-volatile and intermediate volatility primary organic compounds to secondary organic aerosol formation. *Atmos Chem Phys* 10:5491–5514.
14. Robinson AL, et al. (2007) Rethinking organic aerosols: Semivolatile emissions and photochemical aging. *Science* 315:1259–1262.
15. Yu S, Bhave PV, Dennis RL, Mathur R (2007) Seasonal and regional variations of primary and secondary organic aerosols over the continental United States: Semi-empirical estimates and model evaluation. *Environ Sci Technol* 41:4690–4697.
16. Fast J, et al. (2009) Evaluating simulated primary anthropogenic and biomass burning organic aerosols during MILAGRO: Implications for assessing treatments of secondary organic aerosols. *Atmos Chem Phys* 9:6191–6215.
17. Shrivastava M, et al. (2011) Modeling organic aerosols in a megacity: Comparison of simple and complex representations of the volatility basis set approach. *Atmos Chem Phys* 11:6639–6662.
18. Heald CL, et al. (2011) Exploring the vertical profile of atmospheric organic aerosol: Comparing 17 aircraft field campaigns with a global model. *Atmos Chem Phys* 11:12673–12696.
19. Pankow JF (1994) An absorption-model of gas-particle partitioning of organic-compounds in the atmosphere. *Atmos Environ* 28:185–188.
20. Pankow JF (1994) An absorption-model of the gas aerosol partitioning involved in the formation of secondary organic aerosol. *Atmos Environ* 28:189–193.
21. Shiraiwa M, Ammann M, Koop T, Poschl U (2011) Gas uptake and chemical aging of semisolid organic aerosol particles. *Proc Natl Acad Sci USA* 108:11003–11008.
22. Lane TE, Donahue NM, Pandis SN (2008) Simulating secondary organic aerosol formation using the volatility basis-set approach in a chemical transport model. *Atmos Environ* 42:7439–7451.

23. Ezell MJ, et al. (2010) A new aerosol flow system for photochemical and thermal studies of tropospheric aerosols. *Aerosol Sci Technol* 44:329–338.
24. Atkinson R, et al. (2006) Evaluated kinetic and photochemical data for atmospheric chemistry: Volume II—gas phase reactions of organic species. *Atmos Chem Phys* 6:3625–4055.
25. Bonn B, Moortgat GK (2002) New particle formation during α- and β-pinene oxidation by O_3, OH and NO_3, and the influence of water vapour: Particle size distribution studies. *Atmos Chem Phys* 2:183–196.
26. Perraud V, et al. (2010) Identification of organic nitrates in the NO_3 radical initiated oxidation of α-pinene by atmospheric pressure chemical ionization mass spectrometry. *Environ Sci Technol* 44:5887–5893.
27. Wangberg I, Barnes I, Becker KH (1997) Product and mechanistic study of the reaction of NO_3 radicals with α-pinene. *Environ Sci Technol* 31:2130–2135.
28. Berndt T, Böge O (1997) Products and mechanism of the gas-phase reaction of NO_3 radicals with α-pinene. *J Chem Soc Faraday Trans* 93:3021–3027.
29. Hallquist M, Wangberg I, Ljungstrom E, Barnes I, Becker KH (1999) Aerosol and product yields from NO_3 radical-initiated oxidation of selected monoterpenes. *Environ Sci Technol* 33:553–559.
30. Spittler M, et al. (2006) Reactions of NO_3 radicals with limonene and α-pinene: Product and SOA formation. *Atmos Environ* 40:S116–S127.
31. Pankow JF, Asher WE (2008) SIMPOL.1: A simple group contribution method for predicting vapor pressures and enthalpies of vaporization of multifunctional organic compounds. *Atmos Chem Phys* 8:2773–2796.
32. Barnes I, Bastian V, Becker KH, Tong Z (1990) Kinetics and products of the reactions of NO_3 with monoalkenes, dialkenes, and monoterpenes. *J Phys Chem* 94:2413–2419.
33. Socrates G (2001) *Infrared and Raman Characteristic Group Frequencies—Tables and Charts* (Wiley, New York), 3rd Ed.
34. Garnes LA, Allen DT (2002) Size distributions of organonitrates in ambient aerosol collected in Houston, Texas. *Aerosol Sci Technol* 36:983–992.
35. Bruns EA, et al. (2010) Comparison of FTIR and particle mass spectrometry for the measurement of particulate organic nitrates. *Environ Sci Technol* 44:1056–1061.
36. Farmer DK, et al. (2010) Response of the aerosol mass spectrometer to organonitrates and organosulfates and implications for atmospheric chemistry. *Proc Natl Acad Sci USA* 107:6670–6675.
37. Fry JL, et al. (2009) Organic nitrate and secondary organic aerosol yield from NO_3 oxidation of β-pinene evaluated using a gas-phase kinetics/aerosol partitioning model. *Atmos Chem Phys* 9:1431–1449.
38. Rollins AW, et al. (2010) Elemental analysis of aerosol organic nitrates with electron ionization high-resolution mass spectrometry. *Atmos Meas Tech* 3:301–310.
39. Chhabra PS, Flagan RC, Seinfeld JH (2010) Elemental analysis of chamber organic aerosol using an Aerodyne high-resolution aerosol mass spectrometer. *Atmos Chem Phys* 10:4111–4131.
40. Shilling JE, et al. (2009) Loading-dependent elemental composition of α-pinene SOA particles. *Atmos Chem Phys* 9:771–782.
41. Tolocka MP, et al. (2006) Chemistry of particle inception and growth during α-pinene ozonolysis. *Environ Sci Technol* 40:1843–1848.
42. Jang M, Kamens RM (1999) Newly characterized products and composition of secondary aerosols from the reaction of α-pinene with ozone. *Atmos Environ* 33:459–474.
43. Yu JZ, Cocker DR, Griffin RJ, Flagan RC, Seinfeld JH (1999) Gas-phase ozone oxidation of monoterpenes: Gaseous and particulate products. *J Atmos Chem* 34:207–258.
44. Matsunaga A, Ziemann PJ (2009) Yields of β-hydroxynitrates and dihydroxynitrates in aerosol formed from OH radical-initiated reactions of linear alkenes in the presence of NO_x. *J Phys Chem A* 113:599–606.
45. Braun W, Herron JT, Kahaner DK (1988) ACUCHEM: A computer program for modeling complex chemical reaction systems. *Int J Chem Kinet* 20:51–62.
46. Atkinson R, Arey J (2003) Gas-phase tropospheric chemistry of biogenic volatile organic compounds: A review. *Atmos Environ* 37:S197–S219.
47. Ng NL, et al. (2006) Contribution of first- versus second-generation products to secondary organic aerosols formed in the oxidation of biogenic hydrocarbons. *Environ Sci Technol* 40:2283–2297.
48. Chan AWH, Kroll JH, Ng NL, Seinfeld JH (2007) Kinetic modeling of secondary organic aerosol formation: Effects of particle- and gas-phase reactions of semivolatile products. *Atmos Chem Phys* 7:4135–4147.
49. Hall WA, Johnston MV (2011) Oligomer content of α-pinene secondary organic aerosol. *Aerosol Sci Technol* 45:37–45.
50. Tolocka MP, et al. (2004) Formation of oligomers in secondary organic aerosol. *Environ Sci Technol* 38:1428–1434.
51. Ceulemans K, Compernolle S, Peeters J, Muller JF (2010) Evaluation of a detailed model of secondary organic aerosol formation from α-pinene against dark ozonolysis experiments. *Atmos Environ* 44:5434–5442.
52. Adamson AW, Gast AP (1997) *Physical Chemistry of Surfaces* (Wiley, New York), 6th Ed, p 696.
53. Chattopadhyay S, Ziemann PJ (2005) Vapor pressures of substituted and unsubstituted monocarboxylic and dicarboxylic acids measured using an improved thermal desorption particle beam mass spectrometry method. *Aerosol Sci Technol* 39:1085–1100.
54. Yatavelli RLN, Thornton JA (2010) Particulate organic matter detection using a micro-orifice volatilization impactor coupled to a chemical ionization mass spectrometer (MOVI-CIMS). *Aerosol Sci Technol* 44:61–74.
55. Linstrom PJ, Mallard WG, eds. (2011) *NIST Chemistry WebBook, NIST Standard Reference Database Number 69* (National Institute of Standards and Technology, Gaithersburg MD), http://webbook.nist.gov.
56. Ziemann PJ (2010) Atmospheric chemistry: Phase matters for aerosols. *Nature* 467:797–798.
57. Bowman FM, Odum JR, Seinfeld JH (1997) Mathematical model for gas-particle partitioning of secondary organic aerosols. *Atmos Environ* 31:3921–3931.
58. Kamens R, Jang M, Chien CJ, Leach K (1999) Aerosol formation from the reaction of α-pinene and ozone using a gas-phase kinetics aerosol partitioning model. *Environ Sci Technol* 33:1430–1438.
59. Odum JR, Jianzhen Y, Kamens RM (1994) Modeling the mass transfer of semivolatile organics in combustion aerosols. *Environ Sci Technol* 28:2278–2285.
60. Rounds SA, Pankow JF (1990) Application of a radial diffusion model to describe gas/particle sorption kinetics. *Environ Sci Technol* 24:1378–1386.
61. Vaden TD, Song C, Zaveri RA, Imre D, Zelenyuk A (2010) Morphology of mixed primary and secondary organic particles and the adsorption of spectator organic gases during aerosol formation. *Proc Natl Acad Sci USA* 107:6658–6663.
62. Vaden TD, Imre D, Beranek J, Shrivastava M, Zelenyuk A (2011) Evaporation kinetics and phase of laboratory and ambient secondary organic aerosol. *Proc Natl Acad Sci USA* 108:2190–2195.
63. Rounds SA, Tiffany BA, Pankow JF (1993) Description of gas particle sorption kinetics with an intraparticle diffusion-model—desorption experiments. *Environ Sci Technol* 27:366–377.
64. Virtanen A, et al. (2010) An amorphous solid state of biogenic secondary organic aerosol particles. *Nature* 467:824–827.
65. Virtanen A, et al. (2011) Bounce behavior of freshly nucleated biogenic secondary organic aerosol particles. *Atmos Chem Phys* 11:8759–8766.
66. Pierce JR, et al. (2011) Quantification of the volatility of secondary organic compounds in ultrafine particles during nucleation events. *Atmos Chem Phys* 11:9019–9036.
67. Cappa C, Wilson KR (2011) Evolution of organic aerosol mass spectra upon heating: Implications for OA phase and partitioning behavior. *Atmos Chem Phys* 11:1895–1911.
68. Cappa CD, Jimenez JL (2010) Quantitative estimates of the volatility of ambient organic aerosol. *Atmos Chem Phys* 10:5409–5424.
69. Lee BH, Pierce JR, Engelhart GJ, Pandis SN (2011) Volatility of secondary organic aerosol from the ozonolysis of monoterpenes. *Atmos Environ* 45:2443–2452.
70. Stanier CO, Pathak RK, Pandis SN (2007) Measurements of the volatility of aerosols from α-pinene ozonolysis. *Environ Sci Technol* 41:2756–2763.
71. Zobrist B, Marcolli C, Pedernera DA, Koop T (2008) Do atmospheric aerosols form glasses? *Atmos Chem Phys* 8:5221–5244.
72. Mikhailov E, Vlasenko S, Martin ST, Koop T, Poschl U (2009) Amorphous and crystalline aerosol particles interacting with water vapor: Conceptual framework and experimental evidence for restructuring, phase transitions and kinetic limitations. *Atmos Chem Phys* 9:9491–9522.
73. Tong H-J, Reid JP, Bones DL, Luo BP, Krieger UK (2011) Measurements of the timescales for the mass transfer of water in glassy aerosol at low relative humidity and ambient temperature. *Atmos Chem Phys* 11:4739–4754.
74. Koop T, Bookhold J, Shiraiwa M, Poschl U (2011) Glass transition and phase state of organic compounds: Dependency on molecular properties and implications for secondary organic aerosols in the atmosphere. *Phys Chem Chem Phys* 13:19238–19255.
75. Kleinman LI, et al. (2009) The time evolution of aerosol size distribution over the Mexico City plateau. *Atmos Chem Phys* 9:4261–4278.
76. Riipinen I, et al. (2011) Organic condensation: A vital link connecting aerosol formation to cloud condensation nuclei (CCN) concentrations. *Atmos Chem Phys* 11:3865–3878.
77. Yu F (2011) A secondary organic aerosol formation model considering successive oxidation aging and kinetic condensation of organic compounds: Global scale implications. *Atmos Chem Phys* 11:1083–1099.
78. Nieminen T, Lehtinen KEJ, Kulmala M (2010) Sub-10 nm particle growth by vapor condensation—Effects of vapor molecule size and particle thermal speed. *Atmos Chem Phys* 10:9773–9779.
79. Donahue NM, Trump ER, Pierce JR, Riipinen I (2011) Theoretical constraints on pure vapor-pressure driven condensation of organics to ultrafine particles. *Geophys Res Lett* 38:L16801.
80. Bassett ME, Cassmassi JC, Durkee KR, Hogo H (1991) Final air quality and management plan, 1991. Episodic PM-10 model development and application for the South Coast Air Basin. Final Technical Report V-E South Coast Air Quality Management District. (South Coast Air Management District, El Monte, CA).
81. Pilinis C, Seinfeld JH (1988) Development and evaluation of an eulerian photochemical gas aerosol model. *Atmos Environ* 22:1985–2001.
82. Russell LM, Cass GR (1986) Verification of a mathematical model for aerosol nitrate and nitric acid formation, and its use for control measure evaluation. *Atmos Environ* 20:2011–2025.
83. Hogo H, Seignur C, Yocke MA (1985) Draft SCAQMD STAR project working paper No.1: Technical description of a photochemical air quality model with extension to calculate aerosol dynamics and visibility. (South Coast Air Management District, El Monte, CA).
84. Tanner RL (1982) An ambient experimental study of phase-equilibrium in the atmospheric system: Aerosol H^+, NH_4^+,SO_4^{2-}, NO_3-$NH_{3(g)}^-$, $HNO_{3(g)}$. *Atmos Environ* 16:2935–2942.
85. Allen AG, Harrison RM, Erisman JW (1989) Field-measurements of the dissociation of ammonium-nitrate and ammonium-chloride aerosols. *Atmos Environ* 23:1591–1599.
86. Wexler AS, Seinfeld JH (1990) The distribution of ammonium-salts among a size and composition dispersed aerosol. *Atmos Environ* 24:1231–1246.
87. Meng ZY, Dabdub D, Seinfeld JH (1998) Size-resolved and chemically resolved model of atmospheric aerosol dynamics. *J Geophys Res* 103:3419–3435.

Supporting Information

Perraud et al. 10.1073/pnas.1119909109

SI Materials and Methods

Flow Tube Experiments. ***Aerosol flow tube.*** A series of experiments were performed using a unique atmospheric pressure flow system described in detail elsewhere (1). Briefly, the main body of the flow system was a cylindrical stainless steel flow tube of inner diameter 46 cm and length 7.3 m. The first 1.2 m of the flow tube was a mixing section fitted with two types of separate inlets and one downstream inlet for addition of air-diluted O_3, NO_2, and α-pinene, respectively (see below). Reactants and products were well mixed before flowing into a 6.1 m sampling section which was equipped with five equally spaced sampling ports (ports 1–5). The total flow rate into the system was 20 L min^{-1}, which corresponded to a residence time in the flow tube of approximately 1 h. Nitrate radicals were generated from the reaction of 3.3×10^{13} O_3 molecules cm^{-3} (1.4 ppm) with varying concentrations of NO_2 ranging from 0.49×10^{13} to 1.6×10^{14} molecules cm^{-3} (0.2–6.3 ppm). For comparison, an ozonolysis experiment was performed using 3.9×10^{13} O_3 molecules cm^{-3} (1.6 ppm) without added NO_2. For each system, the α-pinene concentration was 2.5×10^{13} molecules cm^{-3} (1.0 ppm). Before each experiment, the flow tube was flushed overnight with a constant flow of dry, filtered compressed air purified by passing through an FTIR purge gas generator (Parker Balston Model 75–62), Carbon/Alumina Media (Perma Pure, LLC), and an inline 0.1 μm filter (DIF-N70; Headline Filters). This purified air was also used for diluting reagents as described below. A typical background concentration of particles in the flow tube before an experiment was <50 particles cm^{-3}.

Reagents. Ozone was generated by passing a 2 L min^{-1} flow of ultrahigh purity oxygen (Oxygen Services, 99.993 %) through a Sander C-100 ozone generator and then diluted with purified air. Ozone in purified dry air entered the upstream end of the flow tube at 10 L min^{-1} and was dispersed across the cross-section of the flow tube using a 16 gauge stainless steel showerhead diffuser disk with many equally spaced holes. Immediately downstream, NO_2 (5,069 ppm in air; Praxair), diluted in purified dry air was injected at 5 L min^{-1} through a spoke-type inlet having a number of openings on the upstream side of each spoke to ensure good mixing of the O_3 and NO_2. As the gas mixture moved downstream, reactions occurred to generate NO_3 and N_2O_5:

$$O_3 + NO_2 \rightarrow NO_3 + O_2 \qquad \textbf{[S1]}$$

$$NO_3 + NO_2 \leftrightarrow N_2O_5. \qquad \textbf{[S2]}$$

α-Pinene [(1*R*)-(+)-*α*-pinene; Sigma-Aldrich, >99%] was added to the $NO_2/O_3/NO_3/N_2O_5$ mixture 55 cm downstream from the addition of NO_2 (corresponding to a reaction time between NO_2 and O_3 of 265 s). Liquid α-pinene was added using a motorized syringe into a constant flow of purified air and through a second spoked-hub inlet at 5 L min^{-1}. Before each experiment, α-pinene was purified by passage through a glass column of neutral aluminum oxide (chromatography grade; J.T. Baker Chemical Company) to remove oxidized impurities. After this treatment, GC/MS analysis showed only a 1.6% β-pinene impurity that was not removed by the aluminum oxide column.

The reaction time between the addition of α-pinene to the $NO_2/O_3/NO_3/N_2O_5$ mixture and the first sampling port (port 1) was 13 min, and the reaction time at the last sampling port (port 5) was 52 min. The relative humidity (RH) in the flow tube was measured to be <3% at both ports (Vaisala humidity and temperature transmitters; models HMT338 and HMP238). Ozone and NO_x concentrations were monitored by a photometric O_3 analyzer (Teledyne Model 400E) and a chemiluminescence NO_x analyzer (Thermo model 42C), respectively. The α-pinene concentrations were analyzed by GC-MS (Hewlett-Packard; 5890 Series II GC and a 5971A Mass Selective Detector equipped with a DB5-ms column of 60-m length, 0.25-mm internal diameter, and a 0.25 μm film thickness (Agilent Technologies, Inc.). Gas samples from the flow tube were pumped through a 10-mL sampling loop (kept at room temperature). Electron impact ionization at 70 eV associated with single ion monitoring (SIM) at m/z 93.10 was used for high sensitivity. Calibration of the instrument was carried out using a certified gas cylinder containing 560 ppb 1S-(−)-*α*-pinene in nitrogen (Scott-Marrin, Inc.).

Particle size distribution measurements. Size distributions of the particles formed from the α-pinene oxidation were measured using a scanning mobility particle sizer (SMPS) configured with a long differential mobility analyzer (DMA; TSI model 3081) and a condensation particle counter (TSI model 3022A), or an aerodynamic particle sizer (APS; TSI model 3321). The SMPS was operated using a sample flow rate of 0.2 L min^{-1}, with a sheath flow of 2 L min^{-1} and a 0.058 cm inlet impactor. Under these conditions, the instrument measured particles with mobility diameters (d_m) ranging from 23 to 965 nm. The APS was operated using a sample flow rate of 5 L min^{-1} and was rated to measure particles with aerodynamic diameters (d_a) from 0.54 to 20 μm. The determination of the number concentration of the particles by their diameter is sensitive to the number of bins into which the selected range is divided (2); in the present experiments, 32 bins were used from the SMPS with the multiple charge correction applied. This binning allowed a smooth pairing of the SMPS to the APS data. The two series of measurements were used to draw a single combined size distribution of the particles. The aerodynamic diameters (d_a) from the APS were converted into electrical mobility diameters (d_m) using Eq. **S3** (3–5)

$$d_m = d_a \sqrt{\chi \frac{C_s(d_a)}{C_s(d_m)} \frac{\rho_o}{\rho_p}} = d_a \sqrt{\frac{\rho_o}{\rho_p}}, \qquad \textbf{[S3]}$$

where C_s is the Cunningham slip correction factor and $C_s(d_a) = C_s(d_m) = 1$ in the continuum regime, χ is the shape factor which is unity for spherical particles (3, 4) and, ρ_p and ρ_o are the densities (g cm^{-3}) of the particle and unit density, respectively. The density of single particles was measured using a single particle mass spectrometer (SPLAT-II). To do so, a DMA (TSI model 3081) was used to select particles with a narrow distribution of particles with 300 nm electrical mobility diameter (d_m) (6). The vacuum aerodynamic diameter (d_{va}) of these size-selected particles was measured using SPLAT-II to obtain information on particle sphericity and high-precision particle densities (6–8). SPLAT-II was also used to measure real-time particle composition as described below.

Real-time particle measurements. Real-time particle composition analysis was performed using both a high-resolution time-of-flight aerosol mass spectrometer (HR-TOF-AMS; Aerodyne Research, Inc.) (9, 10) and SPLAT-II (8). The temperature of the vaporizer in the HR-TOF-AMS was maintained at 230 °C, in an attempt to minimize decomposition of expected organic nitrate products (10). Particle composition information from

SPLAT-II was obtained using two-step laser desorption/ionization of the size-selected particles with a 193 nm excimer laser and an angular reflectron time-of-flight mass spectrometer.

Integrative measurements. Particles were collected at the end of the flow tube using a two-channel sampling line. One channel was equipped with polished ZnSe windows (25 × 2 mm; Reflex Analytical Corporation) enclosed in a modified Sioutas cascade impactor (SKC; model 225-370). Two impactor stages were used at a sampling flow of 9 L min^{-1} with, respectively, 1.0 and 0.5 μm cutoffs (at 9 L min^{-1}). The discs were analyzed by FTIR spectroscopy as described by Bruns et al. (10).

The second channel was equipped with a quartz-fiber filter (Tissuquartz™; 37-mm diameter) mounted in a three-piece polypropylene SureSeal air-monitoring cassette (SKC). Prior to use, the filters were baked in air at 475 °C overnight to remove organic contaminants. Samples from the flow tube passed through a 3-cm diameter by 10-cm-long monolith extruded carbon denuder (Novacarb™; Mast Carbon, Ltd.) installed in front of the filter in order to remove gases from the sample collected at a flow rate of 5 L min^{-1}. Prior to each measurement, the denuders were reconditioned overnight under a stream of ultrahigh purity nitrogen (Oxygen Services Company; 99.995 %) at approximately 75 °C. Independent studies performed to test the efficiency of the denuder showed that the transmission of particles was greater than 92%. The denuder removed more than 95% of N_2O_5/NO_3 at a flow rate of 1 L min^{-1} (11) and more than 99% of O_3 at a flow rate of approximately 6 L min^{-1}. Filter collection efficiency was determined using SMPS and APS measurements before and after the filter. No particles were observed downstream of the filter at a flow rate of 0.2 L min^{-1}. Directly after sampling, the filters were extracted using 2 mL of acetonitrile with sonication for 10 min and analyzed by liquid chromatography with UV detection at 210 nm (LC-UV) using an Agilent HPLC (1100 Series). The LC-UV system was equipped with a 30 mm × 3.2 mm × 5 μm Envirosep PP (Phenomenex) guard column and a 250 mm × 4.6 mm × 5 μm Cyano Microsorb MV (Varian) column both maintained at 35 °C. The sample injection volume was 20 μL. The flow rate was 0.5 mL min^{-1} with the elution gradient from 5% acetonitrile (EMD Chemicals, Inc.; HPLC grade) −95% water (OmniSolv; EMD) to 85% acetonitrile −15% water in 50 min (hold 10 min). Analytes were detected using a diode array detector set at $\lambda = 210$ nm, a wavelength useful for detecting organic nitrates (12–14). 2-Ethylhexyl nitrate (Sigma-Aldrich; 97%) was used as a standard for quantification of the organic nitrates. For each filter extract, the individual contributions were determined using GRAMS/AI8 spectral data processing software (Thermo Electron Corp.) to curve fit the obvious peaks.

PEG Liquid Particle Experiments. PEG particles were generated by nebulizing neat poly(ethylene glycol) (Aldrich; average $M_n \sim$ 400 g mol^{-1}) with a Collison nebulizer (model CN25; BGI) using synthetic air (Oxygen Services Company; blend of O_2 and N_2, THC < 0.01 ppm, H_2O < 2.0 ppm, CO < 0.5 ppm, CO_2 < 0.5 ppm). The total flow of air was 3 L min^{-1} for the nebulizer to operate efficiently. Subsequently, a portion of the flow (1 L min^{-1}) containing the aerosol passed through a vertical glass tube (45 cm in length and 1.9 cm inside diameter), the top half of which was heated with heating tape to approximately 190 °C so as to vaporize PEG and then through the lower unheated half of the tube where the PEG vapor cooled and condensed to form particles with a relatively narrow size distribution (15). The flow of aerosol was then diluted using the same synthetic air (20 L min^{-1}) before being introduced into an approximately 300-L Teflon® reaction chamber.

α-Pinene was injected using a syringe into a 300-L Teflon® reaction chamber initially half-filled with dry synthetic air yielding a concentration of approximately 1 ppm. The RH was measured to be <3% inside the chamber using a Vaisala RH-temperature probe (model HMT338). A N_2O_5/N_2 mixture was then flushed into the same reaction chamber using a flow of dry synthetic air, yielding concentrations of 0.2–0.9 ppm N_2O_5 whose thermal decomposition generated NO_3 radicals. The N_2O_5 was synthesized from the reaction of NO_2 with O_3 followed by trapping in a dry ice-acetone bath and pumping to remove O_2. Further details about the reactants are available (11). After a reaction time of 5 min, PEG particles were added to the Teflon® reaction chamber. The collection of the particles onto a quartz-fiber filter began after 10 min to allow the partitioning of the gas-phase organic nitrate product onto the PEG liquid particles to occur. The size distributions of the particles were also recorded using SMPS.

Evaluation of the Model-Predicted Gas-Phase Concentrations of Organic Nitrate Products. To evaluate the ability of the model to accurately predict the total concentration of organic nitrate products, measurements were performed at port 1 of the flow tube, and compared to the Acuchem model-predicted concentrations for both the organic nitrate products and N_2O_5. Gas-phase samples were analyzed by long-path FTIR in a separate set of experiments where the O_3 and α-pinene are kept constant at 3.4×10^{13} molecules cm^{-3} (1.4 ppm) and 2.5×10^{13} molecules cm^{-3} (1.0 ppm), respectively, and where the NO_2 concentration varied from 2.7×10^{13} molecules cm^{-3} to 1.5×10^{14} molecules cm^{-3} (1.1–6.0 ppm). The long-path FTIR consisted of a Mattson Research Series spectrometer equipped with a long-path glass cell that had a base path of 1 m and an optical path of 64 m. Spectra were recorded at 1 cm^{-1} resolution with 400 co-added scans. Samples were drawn in flow mode from the first port of the flow tube (corresponding to a reaction time of approximately 13 min between α-pinene and the $NO_2/O_3/N_2O_5$ mixture). The gas-phase concentration of N_2O_5 was quantified using the bands at 743 cm^{-1} [cross-section determined to be $(9.03 \pm 0.26) \times 10^{-19}$ cm^2 $molecule^{-1}$ in our laboratory] and 1,246 cm^{-1} (cross-section reported by Hallquist et al., ref. 16, to be 8.56×10^{-19} cm^2 $molecule^{-1}$). Additionally, the organic nitrate products were quantified using the band at 846 cm^{-1} (characteristic of the RO-NO_2 stretch of organic nitrates) and an absorption cross-section of 0.97×10^{-18} cm^2 $molecule^{-1}$ (base 10). This value is the average of the reported cross-sections for two of the major organic nitrates, hydroxypinane nitrate and carbonyl hydroxypinane nitrate, formed in the NO_3 reaction (17).

SI Results and Discussion

Model-Predicted Gas-Phase Concentrations. A simplified 96-step mechanism for the $NO_2 + O_3 + \alpha$-pinene system was developed, and the rate equations integrated using Acuchem (18). The model was first run for the $NO_2 + O_3$ system alone. Their initial concentrations were used in order to calculate the concentrations of all of the species at the α-pinene addition inlet (corresponding to a reaction time of 265 s for the $NO_2 + O_3$ system). The Acuchem model-predicted concentrations of NO_3, O_3, and N_2O_5 (which acts as a reservoir for NO_3 through its thermal decomposition, $N_2O_5 \leftrightarrow NO_3 + NO_2$) are shown in Fig. S1 as a function of the NO_2 initial concentration taken at the point of addition of α-pinene. As the concentration of NO_2 increases, the concentration of O_3 remaining at the α-pinene addition inlet decreases from 3.2×10^{13} to 1.1×10^{13} molecules cm^{-3} (1.3–0.45 ppm). Acuchem also predicts that the NO_3 radicals are mainly "stored" as N_2O_5, whose concentration increases with the NO_2 initial concentration. The predicted concentrations of O_3 and NO_3 are used to determine their relative contributions to the removal of α-pinene at its point of addition. Under all conditions in which NO_2 is present, NO_3 chemistry is the dominant oxidation process, as shown in Table S1. In addition, Table S1 presents the model results when the α-pinene chemistry is added (as specified in the main text). The third column of Table S1 shows that the

NO_3 chemistry is sufficiently rapid that the reaction is >90% complete in terms of α-pinene lost by port 1 (13 min reaction time).

The model is tested by comparing the measured concentrations of the organic nitrates versus the model-predicted concentrations (corresponding to organic nitrates, APONO2, see details of the branching ratio in the text). As presented in Fig. S2, the shape of the dependence of APONO2 concentration on the initial concentration of NO_2 is in good agreement with the total organic nitrate product concentrations measured by long-path FTIR, suggesting that APONO2 is a good proxy for organic nitrates. However, the model systematically overpredicts the values of the organic nitrate product concentrations compared to the measurements by long-path FTIR, which is expected due to the loss of N_2O_5 and organic nitrates on the walls of the flow system and on the sampling lines that is not included in the box model. In addition, an average absorption coefficient at 846 cm^{-1} for all organic nitrates of 9.7×10^{-19} cm^2 $molecule^{-1}$ (base 10) (17) is assumed. Comparison of the box model predictions and measured organic nitrate concentrations shows that the true concentrations of the organic nitrates are 28.5% of the model-predicted values. This correction factor is used in all further calculations involving APONO2.

Particle Size Distributions. Results from SPLAT-II measurements show that the FWHM of the 300-nm size-selected particle aerodynamic diameter distribution lies in the range of 6–6.5% for all experiments, consistent with the particles being spherical (7). In addition, particle density is size-independent and is not dependent on NO_2 concentration. The average density of the particles is 1.205 ± 0.01 (2σ) g cm^{-3} with NO_2 present, and 1.190 g cm^{-3} for the ozone-only experiment. These densities are similar to those reported for organic secondary organic aerosols (SOA) formed from α-pinene ozonolysis (7, 19) as well as from α-pinene photooxidation experiments (20). As a result, Eq. **S3** (see above) can be applied effectively to convert the aerodynamic diameters from the APS into mobility diameters and a combined SMPS-APS can be drawn. The resulting combination of the SMPS and APS measurements is fit using a five-parameter Weibull distribution (21, 22) (Fig. S3):

$$y = y_0 + a\left(\frac{c-1}{c}\right)^{\left(\frac{1-c}{c}\right)}\left|\frac{x-x_0}{b} + \left(\frac{c-1}{c}\right)^{\frac{1}{c}}\right|^{(c-1)} \times \exp\left[-\left|\frac{x-x_0}{b} + \left(\frac{c-1}{c}\right)^{\frac{1}{c}}\right|^{c} + \left(\frac{c-1}{c}\right)\right]. \quad \textbf{[S4]}$$

In Eq. **S4**, y is the particle number concentration (number per cm^{-3}), x is the mobility diameter (d_m in nanometers) and, a, b, c, x_0, and y_0 are five fitting parameters. For each scenario, the SMPS data are used up to 900 nm and data from the APS are used above 1,000 nm. The five-parameter Weibull distribution provides a better fit to the experimental data ($r^2 = 0.83$–0.99 for the Weibull distribution) than the log normal distribution ($r^2 = 0.78$–0.98). Furthermore, the Weibull distribution has been applied successfully to particle distributions in the past (23–26).

Fig. S4 summarizes the number and mass concentrations (calculated using the densities measured by SPLAT-II and the combined SMPS/APS distributions) as well as the geometric mean diameters and geometric standard deviations for the number distributions at port 5. Results are shown for particles collected at port 5 for comparison to the FTIR and filter data; however, in experiments where NO_2 is present, the particle size distributions observed at port 1 are similar to those reported for port 5.

It is noteworthy that both the geometric mean diameter and the geometric standard deviation, a measure of the width of the size distribution, are constant as the NO_2 concentration decreases to 1.1 ppm, and slightly decreases for 0.2 ppm NO_2 (Fig. S4*B*). This absence of a dependence on the NO_2 concentration is consistent with the ozonolysis of α-pinene being the dominant source of new particle formation and growth. As the NO_2 concentration available to react with O_3 is decreased, the concentration of unreacted O_3 increases at the point of addition of the α-pinene; thus the concentration of low volatility ozonolysis products (Prod1) increases and this leads to the formation of more particles through homogeneous nucleation. However, as the same processes and species are involved in all cases, the width of the mass and number distributions remains the same.

Real-Time Aerosol Mass Spectrometry. Fig. S5 shows mass spectra acquired using a HR-TOF-AMS (Fig. S5 *A–D*) and a SPLAT-II (Fig. S5 *E–H*). Both instruments give similar mass spectra showing extensive fragmentation that excludes chemical speciation. Nevertheless, the average particle mass spectra in the presence of NO_2 are similar to those from the ozonolysis, except that the HR-TOF-AMS shows two additional peaks at m/z 30 and 46 primarily from NO^+ and $NO_2{}^+$, whereas SPLAT-II primarily shows the peak at m/z 30. The HR-TOF-AMS data are consistent with previous studies of organic nitrates in SOA (10, 27–29) where the relatively high $NO^+/NO_2{}^+$ ratio is due to the thermal decomposition of organic nitrates under the applied vaporizer temperature (230 °C) (30–32) to form in part ($RO + NO_2$). The high-resolution AMS analysis does not reveal any $C_xH_yN_p{}^+$ ions (organonitrogen ions without oxygen), $HNO_x{}^+$ ions, $NH_x{}^+$ ions, nor ions containing more than one nitrogen in these experiments, but additional minor $C_xH_yO_zN^+$ fragments are identified. However, these fragments contribute less than 5% to the measured sum ($NO^+ + NO_2{}^+ + C_xH_yO_zN^+$).

The HR-TOF-AMS data are analyzed to estimate N/H ratios using the approach of Aiken et al. (33). As described elsewhere (10), the N/H ratio from AMS should be equal to the $n_{(-ONO_2)}/n_{(-CH)}$ ratio estimated from the FTIR spectra, where the ratio of $-ONO_2$ to $-C-H$ groups is estimated from the infrared spectra using the method described previously (10, 34) using the band at 1,280 cm^{-1} (not subject to interference from overlapping peaks). Table S2 compares these two ratios as a function of the initial concentration of NO_2. The N/H ratios range from 0.016 to 0.057, whereas the $n_{(-ONO_2)}/n_{(-CH)}$ ratios vary from 0.04 to 0.11 when NO_2 is present. As discussed previously by Bruns et al. (10), the HR-TOF-AMS systematically underestimates the N/H ratios by factors of 2 to 3 compared to FTIR. A similar discrepancy has been reported using organic standards where the N/H ratios calculated from HR-TOF-AMS data are lower by a factor of 1.3–3 compared to the known N/H ratios (28, 35). The likely source of such a discrepancy is that fragmentation of organic nitrates in the AMS produces neutral NO_x species that are "silent" in the mass spectrometer (10, 13, 14, 36, 37).

The high-resolution capability of the AMS can be used to estimate the O:C atomic ratio which is indicative of the oxidation state of the SOA. As shown in Fig. S6, the O:C ratio is fairly constant over the range of NO_2 concentration, with an average of 0.34 ± 0.10 (±30% error as reported by Aiken et al., ref. 33), suggesting that the average bulk composition of the SOA is not changing dramatically as NO_2 varies. Although the contribution of the individual products to the bulk may change somewhat with NO_2, the HR-TOF-MS and SPLAT-II spectra, and the O:C ratio do not indicate large changes in product distribution. The largest changes in the HR-TOF-MS are at m/z 44 ($C_2H_4O^+ + CO_2{}^+$) and m/z 55 ($C_3H_3O^+$) where the relative intensities increase by a factor of 2 to 3 as the NO_2 decreases to zero. These peaks are attributed to oxidized products such as carboxylic acids that dominate in the ozonolysis reaction. All other peaks changed by less than 25%.

Quantification of the Particulate Organic Nitrate Products. The mass concentration of organic nitrates in the particles (F_i, μg per m^3 of air) is determined from LC-UV analyses using the sum of the

areas of the peaks ($\sum A_{\mathrm{APONO2peaks}}$) in the LC chromatogram (Fig. S7) and Eq. **S5**

$$F_i = \left[\sum A_{\mathrm{APONO2peaks}}\right]\left(\frac{V_{\mathrm{ext}}}{V_{\mathrm{inj}}}\right)\left(\frac{1}{ft}\right)\left(\frac{1}{K_{\mathrm{APONO2}}}\right)\mathrm{MW}_{\mathrm{APONO2}} \qquad \textbf{[S5]}$$

where V_{ext} (microliters) is the final volume of the filter extract, V_{inj} (microliters) is the injection volume into the LC-UV instrument, f ($\mathrm{m^3\ min^{-1}}$) is the air sample flow rate, t (minutes) the sampling time, and $\mathrm{MW}_{\mathrm{APONO2}}$ ($220 \times 10^6\ \mu\mathrm{g\,mol^{-1}}$) is the average molecular weight of the organic nitrates based on a previous study (11). K_{APONO2} (area $\mathrm{mol^{-1}}$) is the molar calibration factor determined using a 2-ethylhexyl nitrate standard (2-EHN) in acetonitrile which has a peak at $t_r = 43$ min. From a previous study, hydroxypinane nitrate, oxo-pinane nitrate, and carbonyl hydroxypinane nitrate species are expected products and these may not have the same calibration factor as 2-EHN (11). For example, Matsunaga and Ziemann (14) reported relative absorptivities of 0.412, 0.964, and 0.608 compared to 2-EHN for authentic samples of β-hydroxynitrate, dihydroxynitrate, and trihydroxynitrate compounds from the oxidation of 2-methyl-alkenes. However, the absolute value of K_{APONO2} will not affect the conclusions reached in the present study regarding the gas-particle partitioning of organic nitrates.

Gas/Particle Partitioning of Organic Nitrates. Activity coefficients (ζ_i) can be estimated from Eq. **S6**) if F_i, A_i, M, $\mathrm{MW_{om}}$ and $p^o_{L,i}$ are known (38, 39),

$$\zeta_i = \frac{RT}{\mathrm{MW_{om}}\,10^6 p^o_{L,j} K_{p,i}} = \frac{RT}{\mathrm{MW_{om}}\,10^6 p^o_{L,i}\left(\frac{F_i/M}{A_i}\right)}, \qquad \textbf{[S6]}$$

where R is the gas constant and T is the temperature. The concentrations F_i and A_i (μg per $\mathrm{m^3}$ of air) of compound i in the aerosol and gas-phase are determined from the LC-UV analysis and the gas-phase kinetics model ($A_i = [\mathrm{APONO2}] - F_i$, where [APONO2] is the corrected concentration defined above), respectively. The total mass (micrograms) of particles per cubic meter of air, M, is known from the SMPS and APS measurements described earlier. The temperature is set at 295 K and $\mathrm{MW_{om}}$ at 200 $\mathrm{g\,mol^{-1}}$ (which is the average molecular mass of the SOA material). The vapor pressure, $p^o_{L,i} = 1.17 \times 10^{-6}$ atm, is an average vapor pressure of organic nitrates identified earlier for the NO_3 reaction with α-pinene (11).

Using these parameters, the values of ζ_i calculated from Eq. **S6** decrease systematically from 7 to 0.5 as the NO_2 concentrations increased from 0.2 to 6.3 ppm. Activity coefficients are often assumed to be unity, but values ranging from less than one to approximately 10^2 have been reported (40). The values depend on the nature of both the compound and the matrix in which it is dissolved (41). As discussed earlier, the HR-TOF-AMS and SPLAT-II data show a similar mass spectral pattern to that from the ozonolysis reaction at all NO_2 concentrations with the addition of peaks due to organic nitrates. Thus, the overall bulk composition of the SOA does not change significantly. Similarly, the LC-UV data show that the nature of the organic nitrate products remains constant with the NO_2 concentration (the intensity of each peaks relative to each other did not change as the NO_2 varies). Thus, the activity coefficients for the organic nitrates in the particles are not expected to vary significantly, nor systematically, with the NO_2 concentration, supporting the conclusion that the variation of F_i/M with A_i is not due to variations in ζ_i.

As discussed in the text, the contribution of organic nitrates to the particle composition is not consistent with equilibrium partitioning into a liquid particle, but rather, with a kinetically limited uptake from the gas-phase to the particles. The excellent agreement between the predicted contribution of organic nitrates to the particles and the measured values is seen in Fig. S8; this plot of the predicted mass fraction of organic nitrates in particles calculated using $\gamma^{\mathrm{APONO2}}/\gamma^{\mathrm{Prod1}} = 0.016$ versus the experimental measurements shows they are highly correlated over all experimental conditions.

Three-Dimensional Airshed Model Calculations Using the University of California, Irvine/California Institute of Technology (UCI-CIT) Model. The UCI-CIT airshed model is a regional air quality model. It has a state-of-the-art chemical mechanism and gas-particle transport modules accounting for organic species partitioning in both the organic and aqueous phase (42). The modeling domain for this study is the South Coast Air Basin of California, discretized with resolutions of 5×5 km in the horizontal direction, and five vertical layers reaching up to 1,100 m in the vertical direction, a maximum boundary layer height developed as based on historical data. The simulation episode is from July 2005, which is part of Study of Organic Aerosols at Riverside campaign, a field study funded by US Environmental Protection Agency and California Air Resources Board (CARB). The corresponding emissions inventory and the meteorological conditions were developed by CARB. A 48-h spin-up period was used to generate the necessary initial conditions at the beginning of each 24-h simulation scenario.

Initially, parent volatile organic compounds i (VOC_i) that can form condensable organic compounds were identified, taking into account several generations of oxidized products. The partitioning of SOA in the base case was first assumed to reach instantaneous equilibrium governed by the equilibrium constant, K_p, where the aerosols in the condensed phase are allowed partition back into the gas phase. These same condensable lumped organic compounds were thus used in the new study case. The updated method for the allocation between the gas and the condensed phase was kinetics driven, and once a product was in the condensed phase, it was not allowed to evaporate back into the gas phase. The kinetically determined SOA production pathway was parameterized with a set of reactions as

$$\text{parent VOC}_i + \text{oxidant} \xrightarrow{k} \beta_i \text{SOA} + (1-\beta_i)\ \text{gas-phase products.} \qquad \textbf{[S7]}$$

That is, a fraction β_i of the reaction gives SOA directly, which is equivalent to assuming that the low-volatility products are irreversibly taken up into particles on a timescale that is fast compared to the rate of product formation (43). The value of β_i, which corresponds to the yield of SOA, will be dependent on the parent VOC_i, but for simplicity, a single value of β_i is assumed. This value of β_i was then varied and $\beta_i = 0.5$–0.6 was observed to generate similar average SOA concentrations to those from field measurements (44). Such large values of β_i suggest an efficient SOA formation from the precursors. Although yields of SOA measured in laboratory studies cover a wide range, there remains considerable controversy regarding their true values in ambient air (45). Clearly there is a need for more laboratory measurements to provide the net uptake coefficient of typical semivolatile organic compounds (SVOCs) found in the atmosphere onto SOA formed from the oxidation of a variety of gas precursors. We recognize that our initial approach does not account for formation of SOA from secondary pathways in the course of VOC oxidation, slow evaporation from the particles (46–48), or contributions from unrecognized VOC precursors (49–51), all of which will also affect SOA formation. In addition, this modeling exercise assumes that equilibrium between the gas phase and particles does not occur, whereas under some conditions in laboratory studies and ambient air, equilibrium between gases and particles may be achieved. However, this equilibrium will be on long timescales if the particles are not liquid; if the timescale is longer than the lifetime of the particles, then equilibrium will not be attained.

1. Ezell MJ, et al. (2010) A new aerosol flow system for photochemical and thermal studies of tropospheric aerosols. *Aerosol Sci Technol* 44:329–338.
2. Chamaillard K, Kleefeld C, Jennings SG, Ceburnis D, O'Dowd CD (2006) Light scattering properties of sea-salt aerosol particles inferred from modeling studies and ground-based measurements. *J Quant Spectrosc Radiat Transfer* 101:498–511.
3. Hinds WC (1999) *Aerosols Technology: Properties, Behavior and Measurement of Airborne Particles* (Wiley Interscience, New York), pp 49–51.
4. DeCarlo PF, Slowik JG, Worsnop DR, Davidovits P, Jimenez JL (2004) Particle morphology and density characterization by combined mobility and aerodynamic diameter measurements. Part 1: Theory. *Aerosol Sci Technol* 38:1185–1205.
5. Khlystov A, Stanier C, Pandis SN (2004) An algorithm for combining electrical mobility and aerodynamic size distributions data when measuring ambient aerosol. *Aerosol Sci Technol* 38:229–238.
6. Zelenyuk A, Cai Y, Chieffo L, Imre D (2005) High precision density measurements of single particles: The density of metastable phases. *Aerosol Sci Technol* 39:972–986.
7. Zelenyuk A, Yang J, Song C, Zaveri RA, Imre D (2008) A new real-time method for determining particles' sphericity and density: Application to secondary organic aerosol formed by ozonolysis of a-pinene. *Environ Sci Technol* 42:8033–8038.
8. Zelenyuk A, Yang J, Choi E, Imre D (2009) SPLAT II: An aircraft compatible, ultra-sensitive, high precision instrument for in-situ characterization of the size and composition of fine and ultrafine particles. *Aerosol Sci Technol* 43:411–424.
9. DeCarlo PF, et al. (2006) Field-deployable, high-resolution, time-of-flight aerosol mass spectrometer. *Anal Chem* 78:8281–8289.
10. Bruns EA, et al. (2010) Comparison of FTIR and particle mass spectrometry for the measurement of particulate organic nitrates. *Environ Sci Technol* 44:1056–1061.
11. Perraud V, et al. (2010) Identification of organic nitrates in the NO_3 radical initiated oxidation of α-pinene by atmospheric pressure chemical ionization mass spectrometry. *Environ Sci Technol* 44:5887–5893.
12. Docherty KS, Ziemann PJ (2006) Reaction of oleic acid particles with NO_3 radicals: Products, mechanism, and implications for radical-initiated organic aerosol oxidation. *J Phys Chem A* 110:3567–3577.
13. Matsunaga A, Ziemann PJ (2009) Yields of β-hydroxynitrates and dihydroxynitrates in aerosol formed from OH radical-initiated reactions of linear alkenes in the presence of NO_x. *J Phys Chem A* 113:599–606.
14. Matsunaga A, Ziemann PJ (2010) Yields of β-hydroxynitrates, dihydroxynitrates, and trihydroxynitrates formed from OH radical-initiated reactions of 2-methyl-1-alkenes. *Proc Natl Acad Sci USA* 107:6664–6669.
15. Liu BYH, Lee KW (1975) Aerosol generator of high stability. *Am Ind Hyg Assoc J* 36:861–865.
16. Hallquist M, Wangberg I, Ljungstrom E, Barnes I, Becker KH (1999) Aerosol and product yields from NO_3 radical-initiated oxidation of selected monoterpenes. *Environ Sci Technol* 33:553–559.
17. Wangberg I, Barnes I, Becker KH (1997) Product and mechanistic study of the reaction of NO_3 radicals with α-pinene. *Environ Sci Technol* 31:2130–2135.
18. Braun W, Herron JT, Kahaner DK (1988) ACUCHEM: A computer program for modeling complex chemical reaction systems. *Int J Chem Kinet* 20:51–62.
19. Bahreini R, et al. (2005) Measurements of secondary organic aerosol from oxidation of cycloalkenes, terpenes, and *m*-xylene using an Aerodyne aerosol mass spectrometer. *Environ Sci Technol* 39:5674–5688.
20. Yu Y, et al. (2008) Photooxidation of α-pinene at high relative humidity in the presence of increasing concentrations of NO_x. *Atmos Environ* 42:5044–5060.
21. Georgopoulos PG, Seinfeld JH (1982) Statistical distribution of air pollutant concentration. *Environ Sci Technol* 16:401A–416A.
22. Johnson NL, Kotz S, Balakrshnan N (1994) *Continuous Univariate Distributions, Volume 1* (Wiley, New York) 2nd Ed, p. 756.
23. Fang ZG, Patterson BR, Turner ME (1993) Modeling particle-size distributions by the Weibull distribution function. *Mater Charact* 31:177–182.
24. Zobeck TM, Gill TE, Popham TW (1999) A two-parameter Weibull function to describe airborne dust particle size distributions. *Earth Surf Processes Landforms* 24:943–955.
25. Smichowski P, et al. (2004) Monitoring trace metals in urban aerosols from Buenos Aires city. Determination by plasma-based techniques. *J Environ Monit* 6:286–294.
26. Cao Q, Tian P, Wu QL (2009) Modeling diameter distributions of poly(N-isopropylacrylamide-co-methacrylic acid) nanoparticles. *J Appl Polym Sci* 111:2584–2589.
27. Alfarra MR, et al. (2006) A mass spectrometric study of secondary organic aerosols formed from the photooxidation of anthropogenic and biogenic precursors in a reaction chamber. *Atmos Chem Phys* 6:5279–5293.
28. Farmer DK, et al. (2010) Response of the aerosol mass spectrometer to organonitrates and organosulfates and implications for atmospheric chemistry. *Proc Natl Acad Sci USA* 107:6670–6675.
29. Fry JL, et al. (2009) Organic nitrate and secondary organic aerosol yield from NO_3 oxidation of β-pinene evaluated using a gas-phase kinetics/aerosol partitioning model. *Atmos Chem Phys* 9:1431–1449.
30. Day DA, Wooldridge PJ, Dillon MB, Thornton JA, Cohen RC (2002) A thermal dissociation laser-induced fluorescence instrument for in situ detection of NO_2, peroxy nitrates, alkyl nitrates, and HNO_3. *J Geophys Res* 107, 10.1029/2001jd000779.
31. Francisco MA, Krylowski J (2005) Chemistry of organic nitrates: Thermal chemistry of linear and branched organic nitrates. *Ind Eng Chem Res* 44:5439–5446.
32. Roberts JM (1990) The atmospheric chemistry of organic nitrates. *Atmos Environ* 24:243–287.
33. Aiken AC, DeCarlo PF, Jimenez JL (2007) Elemental analysis of organic species with electron ionization high-resolution mass spectrometry. *Anal Chem* 79:8350–8358.
34. Sax M, Zenobi R, Baltensperger U, Kalberer M (2005) Time resolved infrared spectroscopic analysis of aerosol formed by photo-oxidation of 1,3,5-trimethylbenzene and α-pinene. *Aerosol Sci Technol* 39:822–830.
35. Rollins AW, et al. (2010) Elemental analysis of aerosol organic nitrates with electron ionization high-resolution mass spectrometry. *Atmos Meas Tech* 3:301–310.
36. Fraser RTM, Paul NC (1968) Mass spectrometry of nitrate esters and related Compounds. Part II. *J Chem Soc B* 1407–1410.
37. Fraser RTM, Paul NC (1968) Mass spectrometry of nitrate esters and related compounds. Part I. *J Chem Soc B* 659–663.
38. Pankow JF (1994) An absorption-model of gas-particle partitioning of organic-compounds in the atmosphere. *Atmos Environ* 28:185–188.
39. Pankow JF (1994) An absorption-model of the gas aerosol partitioning involved in the formation of secondary organic aerosol. *Atmos Environ* 28:189–193.
40. Jang M, Kamens RM, Leach KB, Strommen MR (1997) A thermodynamic approach using group contribution methods to model the partitioning of semivolatile organic compounds on atmospheric particulate matter. *Environ Sci Technol* 31:2805–2811.
41. Bowman FM, Melton JA (2004) Effect of activity coefficient models on predictions of secondary organic aerosol partitioning. *J Aerosol Sci* 35:1415–1438.
42. Chang WL, Griffin RJ, Dabdub D (2010) Partitioning phase preference for secondary organic aerosol in an urban atmosphere. *Proc Natl Acad Sci USA* 107:6705–6710.
43. Bowman FM, Odum JR, Seinfeld JH (1997) Mathematical model for gas-particle partitioning of secondary organic aerosols. *Atmos Environ* 31:3921–3931.
44. Docherty KS, et al. (2008) Apportionment of primary and secondary organic aerosols in Southern California during the 2005 study of organic aerosols in Riverside (SOAR-1). *Environ Sci Technol* 42:7655–7662.
45. Matsunaga A, Ziemann PJ (2010) Gas-wall partitioning of organic compounds in a Teflon film chamber and potential effects on reaction product and aerosol yield measurements. *Aerosol Sci Technol* 44:881–892.
46. Vaden TD, Imre D, Beranek J, Shrivastava M, Zelenyuk A (2011) Evaporation kinetics and phase of laboratory and ambient secondary organic aerosol. *Proc Natl Acad Sci USA* 108:2190–2195.
47. Cappa C, Wilson KR (2011) Evolution of organic aerosol mass spectra upon heating: Implications for OA phase and partitioning behavior. *Atmos Chem Phys* 11:1895–1911.
48. Rounds SA, Tiffany BA, Pankow JF (1993) Description of gas particle sorption kinetics with an intraparticle diffusion-model—desorption experiments. *Environ Sci Technol* 27:366–377.
49. Chung MY, Maris C, Krischke U, Meller R, Paulson SE (2003) An investigation of the relationship between total nonmethane organic carbon and the sum of speciated hydrocarbons and carbonyls measured by standard GC/FID: Measurements in the Los Angeles air basin. *Atmos Environ* 37:S159–S170.
50. Chatani S, et al. (2009) Sensitivity analyses of OH missing sinks over Tokyo metropolitan area in the summer of 2007. *Atmos Chem Phys* 9:8975–8986.
51. Sadanaga Y, Yoshino A, Kato S, Kajii Y (2005) Measurements of OH reactivity and photochemical ozone production in the urban atmosphere. *Environ Sci Technol* 39:8847–8852.

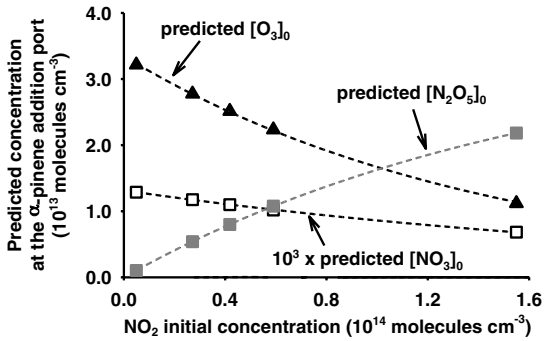

Fig. S1. Model-predicted concentrations of NO_3, O_3, and N_2O_5 at the α-pinene addition port as a function of the initial concentration of NO_2. For each species, the dotted line represents the results from Acuchem and the symbols (black triangles, white squares, gray squares) indicate the concentrations at which the experiments are performed.

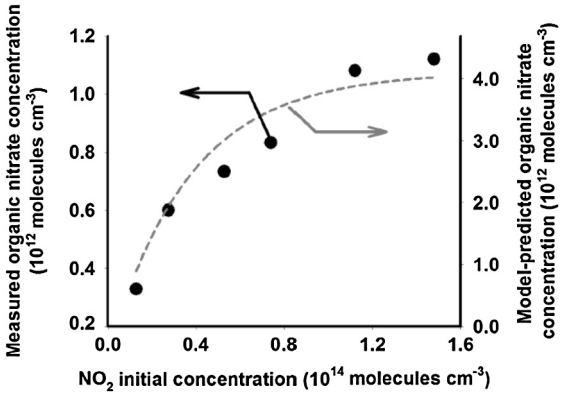

Fig. S2. Model-predictions of organic nitrate concentrations (gray dashed line) versus measurements by long-path FTIR (black circles).

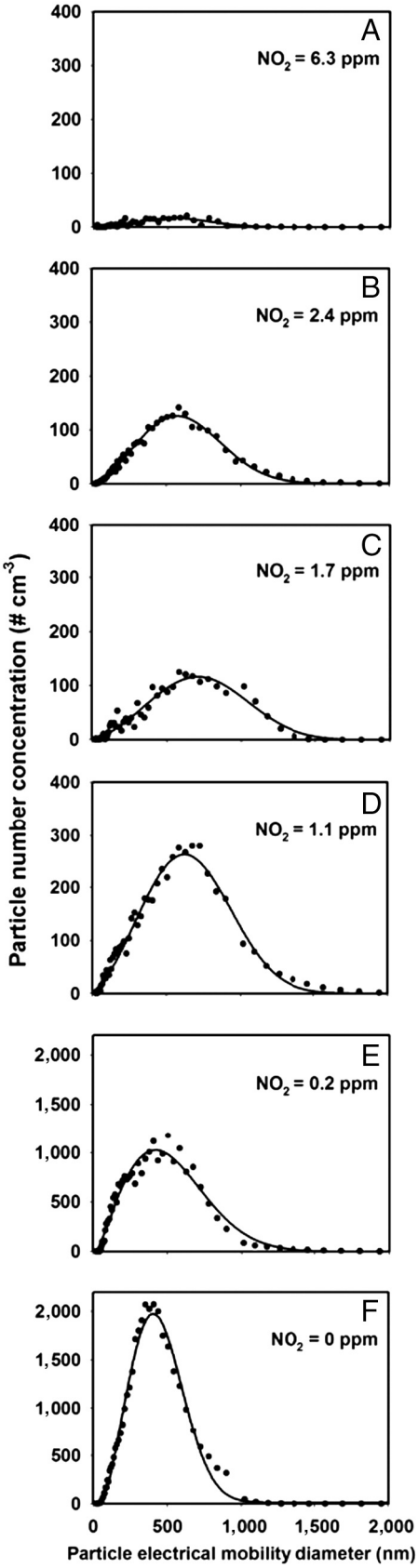

Fig. S3. Combined SMPS-APS size distributions of particles as a function of NO_2 concentration from (*A*) 6.3 ppm to (*E*) 0.2 ppm. *F* shows data from the ozonolysis of α-pinene with 1.6 ppm O_3. Measurements were made at port 5 of the flow tube (*ca.* 52 min reaction time between α-pinene and the $NO_2/O_3/N_2O_5$ mixture) except for *D*, where only SMPS data from port 1 were available (*ca.* 13 min reaction time between α-pinene and the $NO_2/O_3/N_2O_5$ mixture). When simultaneous measurements were made at port 1 and port 5 for the $NO_2 + O_3$ system, the measured distributions were similar.

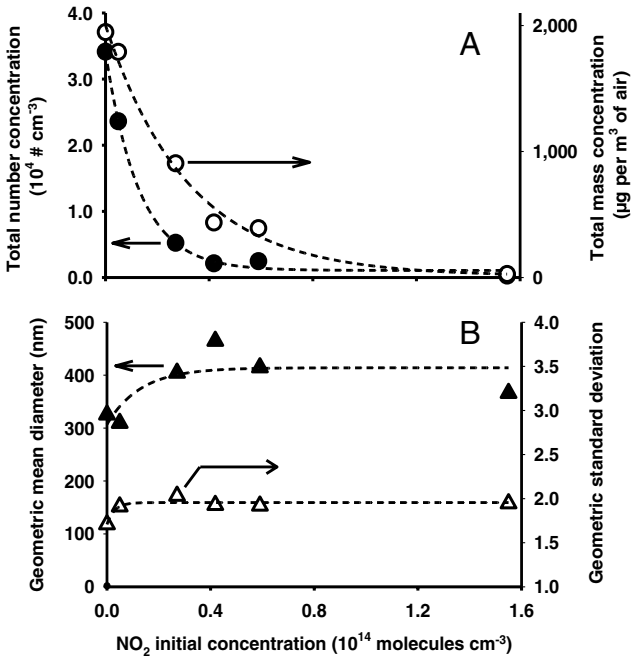

Fig. S4. (*A*) Total number (black circles) and mass (open circles) concentrations of particles; and (*B*) geometric mean diameter (black triangles) and geometric standard deviation (open triangles) of particles as a function of NO_2 initial concentration.

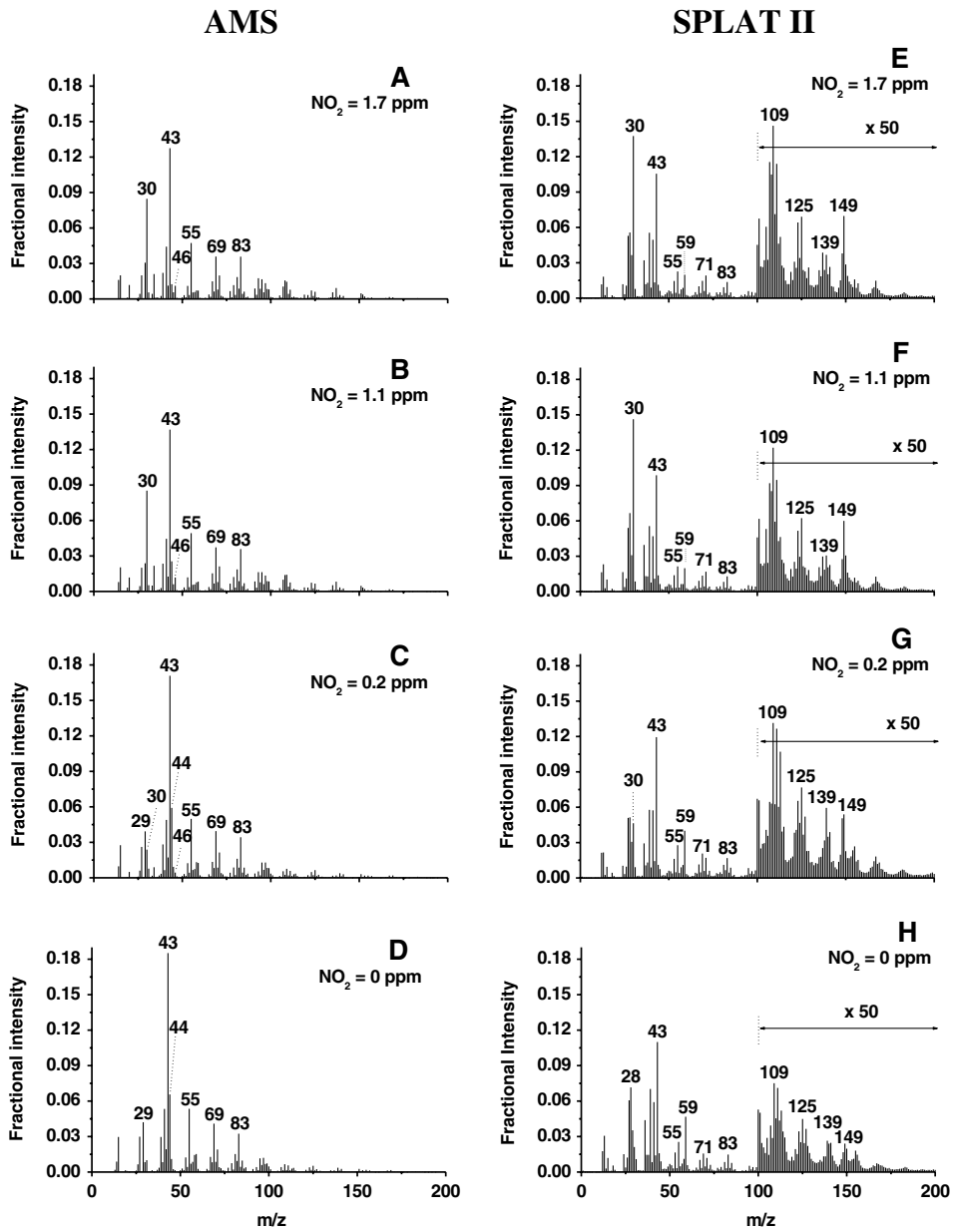

Fig. S5. HR-TOF-AMS (*A–D*) and SPLAT-II (*E–H*) mass spectra of particles as a function of the initial NO_2 concentration. The HR-TOF-AMS measurements were for all particles (40 nm–1 μm) and the SPLAT-II measurements were on size-selected 300-nm particles. All intensities are normalized to the total MS signals. In the HR-TOF-AMS mass spectra, the air beam peaks have been removed.

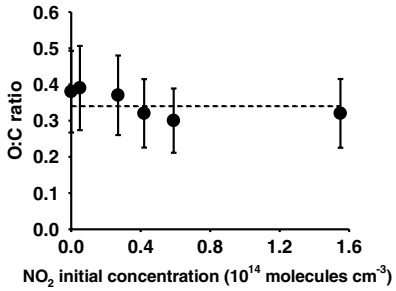

Fig. S6. Oxygen to carbon atomic ratio from the high-resolution data analysis of the AMS spectra as a function the initial concentration of NO_2 (which determines the NO_3 radicals available to react with α-pinene). The dotted line represents the average O:C ratio of 0.34. The error bars on the O:C ratio are 30% based on Aiken et al. (33).

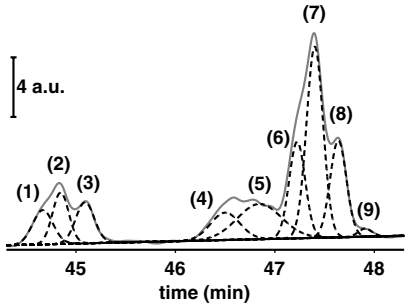

Fig. S7. Typical LC-UV chromatogram of a filter extract obtained from an experiment with $NO_2 = 2.4$ ppm. Filters were extracted using 2 mL acetonitrile and analyzed by LC-UV using a detection at $\lambda = 210$ nm, specific to organic nitrates. Because separation of the individual organic nitrate products was not achieved under the applied chromatographic conditions, GRAMS/AI8 spectral data processing software (Thermo Electron Corp.) was used to curve fit the trace. It is noteworthy that the resulting number of peaks fitted may not correspond necessarily to the number of individual organic nitrate products. From a previous study (11), three of the peaks should correspond to hydroxypinane nitrate, oxo-pinane nitrate, and carbonyl hydroxypinane nitrate, but the other peaks remain unassigned. Nevertheless, all the peaks had UV spectra characteristic of organic nitrates, and no peaks were observed at these retention times in the solvent blanks.

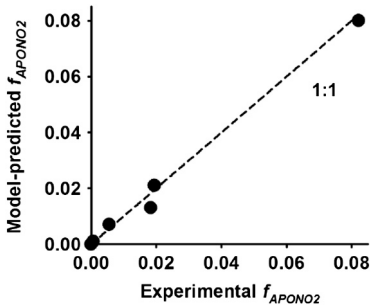

Fig. S8. Model-predicted mass fraction of organic nitrates in particles using relative uptake coefficients $\gamma^{APONO2}/\gamma^{Prod1} = 0.016$ compared to the experimentally measured values. The model-predicted mass fraction of organic nitrate were estimated using [APONO2] and [Prod1] from the box model, and $MW_{APONO2} = 220$ g mol^{-1} (26) and $MW_{Prod1} = 200$ g mol^{-1}). The 1:1 slope supports the derived value of 0.016 for the relative uptake coefficients.

Table S1. Model-predicted kinetics and loss of α-pinene at port 1

Initial $[NO_2]_0$ 10^{14} molecules cm^{-3} or [ppm]	Predicted kinetics at the α-pinene addition inlet: $\frac{k^{NO_3}[NO_3]_0}{k^{O_3}[O_3]_0}$	% of α-pinene unreacted at port 1
	NO_3 experiments, with $[O_3]_0 = 1.4$ ppm	
1.6 [6.3]	42	0.03
0.59 [2.4]	31	0.16
0.42 [1.7]	30	0.91
0.27 [1.1]	29	3.9
0.05 [0.2]	28	9.0
	O_3 experiments, with $[O_3]_0 = 1.6$ ppm	
0.00	0	6.8

Rate constants k^{NO_3} (6.2×10^{-12} cm^3 molecule^{-1} s^{-1}) and k^{O_3} (9.0×10^{-17} cm^3 molecule^{-1}s^{-1}) from Atkinson et al. (1) and NO_3 and O_3 concentrations from the model-predictions at the point of addition of α-pinene.

1. Atkinson R, et al. (2006) Evaluated kinetic and photochemical data for atmospheric chemistry: Volume II—gas-phase reactions of organic species. *Atmos Chem Phys* 6:3625–4055.

Table S2. Quantification of nitrogen in particles from high-resolution AMS analysis and from FTIR spectra analysis

Initial $[NO_2]_0$ 10^{14} molecules cm^{-3} or [ppm]	HR-TOF-AMS* N/H	FTIR* $n_{(-ONO_2)}/n_{(-CH)}$
	NO_3 experiments, with $[O_3]_0 = 1.4$ ppm	
1.6 [6.3]	0.057	0.11
0.59 [2.4]	0.030	0.077
0.42 [1.7]	0.046	0.089
0.27 [1.1]	0.047	0.081
0.05 [0.2]	0.016	0.040
	O_3 experiments, with $[O_3]_0 = 1.6$ ppm	
0.00	0.004	0

*The ratios measured by these two approaches are expected to be the same.